

# Mass and Concentration estimates from Weak and Strong Gravitational Lensing: a Systematic Study

Carlo Giocoli<sup>1,2,3\*</sup>, Massimo Meneghetti<sup>2,3,4</sup>, R. Benton Metcalf<sup>1</sup>, Stefano Ettori<sup>2,3</sup>, Lauro Moscardini<sup>1,2,3</sup>

<sup>1</sup> *Dipartimento di Fisica e Astronomia, Alma Mater Studiorum Università di Bologna, viale Bertini Pichat, 6/2, 40127 Bologna, Italy*

<sup>2</sup> *INAF - Osservatorio Astronomico di Bologna, via Ranzani 1, 40127, Bologna, Italy*

<sup>3</sup> *INFN - Sezione di Bologna, viale Bertini Pichat 6/2, 40127, Bologna, Italy*

<sup>4</sup> *Jet Propulsion Laboratory, 4800 Oak Grove Dr. Pasadena, CA 91109, USA*

2 March 2022

## ABSTRACT

We study how well halo properties of galaxy clusters, like mass and concentration, are recovered using lensing data. In order to generate a large sample of systems at different redshifts we use the code MOKA. We measure halo mass and concentration using weak lensing data alone (WL), fitting to an NFW profile the reduced tangential shear profile, or by combining weak and strong lensing data, by adding information about the size of the Einstein radius (WL+SL). For different redshifts, we measure the mass and the concentration biases and find that these are mainly caused by the random orientation of the halo ellipsoid with respect to the line-of-sight. Since our simulations account for the presence of a bright central galaxy, we perform mass and concentration measurements using a generalized NFW profile which allows for a free inner slope. This reduces both the mass and the concentration biases. We discuss how the mass function and the concentration mass relation change when using WL and WL+SL estimates. We investigate how selection effects impact the measured concentration-mass relation showing that strong lens clusters may have a concentration 20 – 30% higher than the average, at fixed mass, considering also the particular case of strong lensing selected samples of relaxed clusters. Finally, we notice that selecting a sample of relaxed galaxy clusters, as is done in some cluster surveys, explain the concentration-mass relation biases.

**Key words:** galaxies: halos - cosmology: theory - dark matter - methods: analytical - gravitational lensing: weak and strong

## 1 INTRODUCTION

Galaxy clusters represent a very important cosmological laboratory. Their abundance and evolution is related to important cosmological parameters. To first order, the cluster counts as a function of redshift mainly depend on the matter density of the universe  $\Omega_m$ , the dark energy equation of state parameter  $w$  and the normalization of the initial power spectrum of density fluctuations,  $\sigma_8$ . In the era of precision cosmology, and with the advent of future wide field surveys, new and independent cosmological probes are necessary for disentangling degeneracies between some cosmological parameters.

In particular, in order to use the cluster mass function as a cosmological probe it is necessary to be able to

estimate their mass with very high accuracy. Observations in different wavelengths provide different, indirect measurements of cluster mass that can be compared or combined with each other. Many clusters have been observed in both X-ray (CHANDRA and XMM) (Ettori et al. 2009, 2010) and optical and near-IR (HST, SUBRAU and VLT) (Newman et al. 2009, 2011). Using X-ray data it is possible to extract the cluster mass from the observed brightness and gas temperature profiles by assuming spherical symmetry and hydrostatic equilibrium (Ettori et al. 2013). However, some biases might affect the estimated mass due to unresolved non-thermal contribution to the total gas pressure Rasia et al. (2006, 2012). In a recent paper (Planck Collaboration et al. 2013) the Planck collaboration has presented the constraints on cosmological parameters ( $\Omega_m$  and  $\sigma_8$ ) using number counts as a function of redshift for a sample of 189 galaxy clusters selected thanks to their Sunyaev-Zeldovich signal. The authors point out that the measured cosmologi-

\* E-mail: carlo.giocoli@unibo.it

cal parameters are degenerate with the hydrostatic mass bias and that only a bias of about 45% can reconcile the measured  $\sigma_8$  from cluster counts with the one measured from the primary CMB anisotropies (although see Hajian et al. (2013)).

Optical and near-IR data allow one to measure the (weak and strong) lensing signal of background galaxies. The mass and the critical lines can be recovered from elongated arcs and multiple images. Conversely, estimating the cluster mass is also very important for predicting the redshift of the arcs and to identify highly magnified high redshift galaxies (Coe et al. 2013) – recall that the size of the critical curve depends on the redshift of the source (Zieser & Bartelmann 2012; Zitrin et al. 2013b).

These estimates can be turned into indirect measurements of the projected mass distribution of the cluster along the line of sight, and then into an estimate of the virial mass of the system (Hoekstra 2003; Meneghetti et al. 2010b; Hoekstra et al. 2013). Many studies have shown inconsistencies between the mass estimated from X-ray and lensing observables (Meneghetti et al. 2010b; Rasia et al. 2012), mainly because clusters are not spherical or relaxed system and contain substructures – cluster members. It is also reasonable to suspect that clusters with strong lensing features preferentially have their major axis oriented along the line of sight (Sereno & Zitrin 2012) or very elongated in the plane of the sky (Zitrin et al. 2013a,b) – also because in merging or post merging phase, which breaks down the usual assumption of spherical symmetry when deprojecting the mass model from two to three dimensions (Limousin et al. 2013).

By combining the estimated mass and concentration of observed clusters we can measure the mass-concentration relation and compare it with the predictions extracted from numerical simulations. However, it is worth noting that many studies are finding a mass-concentration relation that tends to be higher than what is expected from dark matter only  $N$ -body simulations (Rasia et al. 2013). However, it should be emphasized that the cooling of baryons is expected to make haloes more concentrated through adiabatic contraction while at the same time an uncertain amount of feedback from the central AGN can partially counteract this contraction (Killedar et al. 2012; Fedeli 2012).

Several systematic errors contribute to a scatter and bias in the estimated cluster masses from lensing. The presence of such systematics can be seen directly in the data. For example, the mass obtained for a single cluster using different source galaxy samples differs by  $\sim 10\%$ . The estimated masses also depend on the radial range over which the fit is performed. Applegate et al. (2012) suggest that a range at least out to  $2 \times R_{500}$  should be used. What mass model is used in the fit can also affect the result. Applegate et al. (2012) fix the concentration while Okabe et al. (2013) consider it as a parameter to be estimated from the fit. In addition, there are systematics arising from the assumed mass model, shear calibration and background galaxy redshift distribution. Mahdavi et al. (2013), estimating the hydrostatic and the weak lensing mass of a sample of 50 clusters, noticed that hydrostatic masses underestimate weak lensing masses by 10% on average, within  $R_{500}$ .

The mass estimates of strong lensing selected clusters are typically uncertain to within 30% (Bartelmann & Steinmetz 1996b) because of substructures and projection ef-

fects. More recent analyses by Kneib & Natarajan (2011); Meneghetti et al. (2010b) show that the estimates of cluster core masses from strong lensing are accurate to within 10%. For comparison, mass estimates from X-ray observations are biased low with respect to lensing masses by around 25% because they assume hydrostatic equilibrium (Meneghetti et al. 2010b; Rasia et al. 2012). However it is important to note that X-ray and lensing (weak plus strong) analyses can be combined in such a way as to resolve the degeneracy between mass and elongation (Morandi et al. 2010).

In this work we will address where systematic effects arise when trying to estimate the mass and the concentration from lensing data, considering the contributions coming from the halo triaxiality and orientation, and from the presence of substructures and/or the bright central galaxy.

Another complication when estimating the mass and concentration of halos from lensing comes from the presence of objects along the line of sight that are unrelated to the halo being considered. This is a relatively unexplored source of systematic error. In this paper we will consider only substructures in the main halo. In a subsequent paper we will address the effects of line of sight structures.

The paper is organized as follows. In Section 2 we describe our lens model and explain how we extract from each simulated cluster weak and strong lensing information. Section 3 is dedicated to present how well mass and concentration are recovered using as a reference a Navarro et al. (1996) (NFW) model to fit the lensing data, while in Section 4 we investigate the case of a generalized NFW model. In Section 5 we present the results for a cosmological sample of clusters and discuss how mass and concentration uncertainties are reflected in the halo mass function and in the concentration mass-relation. In Section 6 we summarize our finding.

## 2 THE METHOD

In order to create a large sample of triaxial and substructured convergence maps of galaxy-cluster size haloes we make use of the code MOKA<sup>1</sup> (Giocoli et al. 2012a). MOKA builds up the convergence map of haloes in an analytical way, treating them as made up of three components: (i) the main halo – assumed to be smooth, triaxial, with an NFW profile (in the code has been also implemented the possibility to use a generalized-NFW profile), (ii) the cluster members – subhaloes, distributed to follow the main halo and to have a truncated Singular Isothermal Sphere profile (Metcalf & Madau 2001) – and (iii) the brightest cluster galaxy (BCG) modelled with a Hernquist (1990) profile (in MOKA a Jaffe (1983) model for the BCG has also been implemented). The axial ratios,  $a/b$  and  $a/c$ , of the main halo ellipsoid are randomly drawn from the Jing & Suto (2002) distributions requiring  $abc = 1$ . The halo ellipsoid is randomly oriented choosing a point on a sphere identified by its azimuthal and elevation angles. We assign the same projected ellipticity to the smooth component, to the stellar density and to the subhalo spatial distribution. This is motivated by the hierarchical clustering scenario where the

<sup>1</sup> <http://giocoli.wordpress.com/research-interests/moka>

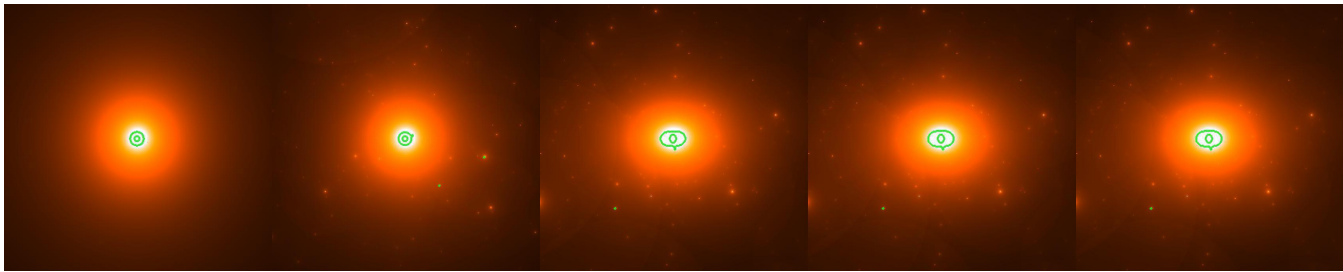


**Figure 1.** Convergence map of a cluster with virial mass of  $M_{vir} = 5 \times 10^{14} M_{\odot}/h$  and concentration  $c_{vir} = 6$  located at redshift  $z = 0.288$  and sources placed at redshift  $z_s = 2$ . In the first panel on the left we show the spherical halo without substructures, while they are included in the second panel. In the third panel we assign a 3D ellipticity to the main halo ellipsoid and randomly rotate it with respect to the line of sight; in the fourth and fifth panel we consider also the presence of a BCG located at the centre of the cluster with the difference that in the latter we account also for adiabatic contraction of the dark matter. In each panel the green curve in the central region defines the location of the critical curves, where the magnification  $\mu$  is infinite.

BCG and the substructures are related to the cluster as a whole and retain memory of the directions of the accretion of repeated merging events (Kazantzidis et al. 2004, 2008, 2009; Fasano et al. 2010). In our simulations, we also account for the adiabatic contraction of the dark matter caused by the BCG. We have implemented the adiabatic contraction as described by Keeton (2001) both for the Hernquist (1990) and the Jaffe (1983) profiles. For more details about the MOKA code we refer to Giocoli et al. (2012a,c). The code also takes into account the correlation between assembly history and different halo properties: (i) less massive haloes typically tend to be more concentrated than the more massive ones, and (ii) at fixed mass, earlier forming haloes are more concentrated and less substructured. These recipes have been implemented considering the recent results from numerical simulations. In particular, we assume the Zhao et al. (2009) relation to link the concentration to mass and the Giocoli et al. (2010a) relation for the subhalo abundance. When substructures are included we define smooth mass as  $M_{smooth} = M_{vir} - \sum_i m_{sub,i}$  and its concentration  $c_s$  is set in such a way that the total (smooth+clumps) mass density profile has a concentration  $c_{vir}$ , equal to the original one.

Throughout the paper we will denote with  $M_{vir}$  (or  $M_{3D}$ ) the cluster mass and with  $c_{vir}$  (or  $c_{3D}$ ) the halo concentration. For these definitions we assume the one adopted for the spherical collapse model:

$$M_{vir} = \frac{4\pi}{3} R_{vir}^3 \frac{\Delta_{vir}}{\Omega_m(z)} \Omega_0 \rho_c, \quad (1)$$

where  $\rho_c = 2.77 \times 10^{11} h^2 M_{\odot}/\text{Mpc}$  represents the critical density of the Universe,  $\Omega_0 = \Omega_m(0)$  is the matter density parameter at the present time,  $\Delta_{vir}$  is the virial overdensity (Eke et al. 1996; Bryan & Norman 1998) and  $R_{vir}$  symbolizes the virial radius of the halo, i.e. the distance from the halo centre that encloses the desired density contrast; and:

$$c_{vir}(M_{vir}, z) \equiv \frac{R_{vir}}{r_s} = 4 \left\{ 1 + \left[ \frac{t(z)}{3.75 t_{4\%}} \right]^{8.4} \right\}^{1/8}, \quad (2)$$

with  $r_s$  the radius at which the NFW profile approaches a logarithmic slope of  $-2$ ,  $t(z)$  is the cosmic time corresponding at redshift  $z$  and  $t_{4\%}$  the one at which the main halo progenitor assembles 4% of its mass (Zhao et al. 2009; Giocoli et al. 2012b).

The characterization of galaxy cluster properties done

in this way is simplified, but on average resembles – in the best way – the properties measured from numerical simulations. Since we are interested in discussing only the average lensing properties of a large sample of systems, we do not include in this work more particular asymmetries present in galaxy clusters.

The whole halo catalogue is made up by galaxy clusters above  $10^{14} M_{\odot}/h$  at six different redshifts ( $z = 0.187, 0.288, 0.352, 0.450, 0.548$  and  $0.890$ ) with sources located at  $z_2 = 2$ . To make our results easily comparable to recent observational data, these redshifts have been chosen to match those of some clusters observed during the CLASH program (Postman et al. 2012): Abell 383, Abell 611, MACS1115.9+0129, RXJ1347.5-1145, MACS0717.5+3745 and CLJ1226.9+3332. For each redshift, we generate in total 12288 cluster maps from  $10^{14}$  to  $3.16 \times 10^{15} M_{\odot}/h$ , with a constant bin size of  $d \log(M) = 0.25$ , creating 2048 maps for each considered bin.

## 2.1 WL and SL signals from the simulated clusters

Because of their mass density distribution, triaxiality and baryon content, galaxy clusters represent interesting gravitational lenses, deflecting the light rays from background galaxies. Observing the source images, we can typically distinguish two different lensing regimes: one in the outer regions, where the images of background galaxies appear slightly distorted and magnified, called weak gravitational lensing (WL) (Bartelmann & Schneider 2001), and one in the central part, where background sources are highly magnified, distorted and multiply imaged, called strong gravitational lensing (SL) (Kneib & Natarajan 2011; Meneghetti et al. 2013).

In Fig. 1, we show, as an example, the projected density map of one of our clusters with virial mass  $M_{vir} = 5 \times 10^{14} M_{\odot}/h$  and concentration  $c_{vir} = 6$  located at redshift  $z = 0.288$ . In the first panel on the left we present the case in which the halo is perfectly smooth and spherical. In the second panel the halo contains substructures whose mass function resembles the one obtained by Giocoli et al. (2010a) from a cosmological numerical simulation. In the third panel, we introduce triaxiality to the smooth component and to the satellite spatial distribution, and randomly orient the major

axis with respect to the line of sight. The forth panel shows the projected density map of the cluster where the BCG is included, finally in the fifth panel the adiabatic contraction of the dark matter is also considered. The median distance of the tangential critical points  $\theta_E$  – that we will introduce later in the text, increases from left to right and assumes the following values:

$$\theta_E = 8.2, 7.9, 11.4, 11.7, 12.4 \text{ arcsec} . \quad (3)$$

The small changes of the Einstein radius when substructures are included is due to the redistribution of the virial mass between the smooth and the clump components.

From the projected density  $\Sigma(r) = \int \rho(r, z) dz$ , we can define the convergence as:

$$\kappa(r) = \frac{\Sigma(r)}{\Sigma_{\text{crit}}}, \quad \text{with} \quad \Sigma_{\text{crit}} = \frac{c^2}{4\pi G} \frac{D_l}{D_s D_{ls}} .$$

where  $c$  represents the speed of light and  $G$  the universal gravitational constant;  $D_l$ ,  $D_s$  and  $D_{ls}$  are the angular diameter distances observer-lens, observer-source and source-lens, respectively. Using the convergence, we can define the effective potential  $\Phi(x, y)$ , the scaled deflection angle  $\alpha(x, y)$  and introduce the pseudo-vector field of the shear using the complex notation,  $\gamma = \gamma_1 + i\gamma_2$  by its components:

$$\gamma_1(x, y) = \frac{1}{2} (\Phi_{11} - \Phi_{22}) \quad (4)$$

and

$$\gamma_2(x, y) = \Phi_{12} = \Phi_{21}; \quad (5)$$

from which we can define the tangential and the cross components of the shear

$$\gamma_t = -[\gamma_1 \cos(2\phi) + \gamma_2 \sin(2\phi)] \quad (6)$$

$$\gamma_\times = -\gamma_1 \sin(2\phi) + \gamma_2 \cos(2\phi), \quad (7)$$

respectively. These components are respectively perpendicular and parallel to the radius vector;  $\phi$  specifies the angles with respect to the centre of the coordinate frame; in what follows we will denote with  $g$  the reduced shear as:

$$g \equiv \frac{\gamma}{1 - \kappa}. \quad (8)$$

The reduced shear, and not the actual shear, is the observable quantity from image ellipticities (Bartelmann & Schneider 2001; Viola et al. 2011). We recall that in the weak lensing regime the tangential shear is related to the mass density through the relation:  $\gamma_t(\theta) = \bar{\kappa}(<\theta) - \kappa(\theta)$ . From the definitions of the tangential and cross components of the shear we can compute the corresponding reduced shear quantities  $g_t$  and  $g_\times$  that are related to the corresponding components of the image ellipticity  $\epsilon_t$  and  $\epsilon_\times$  of background sources (Bartelmann & Schneider 2001). In the absence of higher order effects, the azimuthal average of the cross component ( $\gamma_\times$ ) is expected to vanish. In practice, the presence of cross modes can be used to check for systematic errors.

The differential deflection of light bundles propagating from the source to the observer are given by to the Jacobian matrix:

$$A = (\delta_{ij} - \Phi_{ij}) = \begin{pmatrix} 1 - \kappa - \gamma_1 & -\gamma_2 \\ -\gamma_2 & 1 - \kappa - \gamma_1 \end{pmatrix}, \quad (9)$$

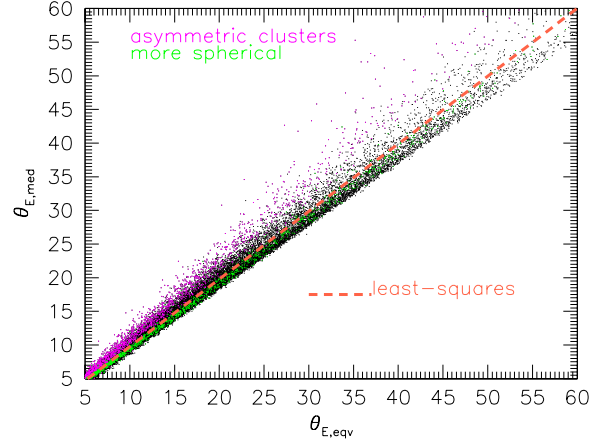


**Figure 2.** Correlation between the median and the equivalent Einstein radius definitions for the whole sample of haloes above  $10^{14} M_\odot/h$  at the six considered redshifts. The dashed line shows the least-squares fit to the data, and is almost equivalent with the bisector. The magenta points show the relation for clusters with a convergence ellipticity within  $R_{2500}$   $\epsilon_{\kappa,2500} > 0.7$ , while the green points for clusters with  $\epsilon_{\kappa,2500} < 0.1$ .

with eigenvalues

$$\lambda_t = 1 - \kappa - \gamma \quad (10)$$

and

$$\lambda_r = 1 - \kappa + \gamma. \quad (11)$$

The cases  $\lambda_r = 0$  and  $\lambda_t = 0$  define the location of radial and tangential critical lines in the lens plane; where the magnification  $\mu$  is infinite (green lines in Fig. 1). In order to define the Einstein radius of the lens, we consider all the points in the lens plane with  $\lambda_t = 0$  and connect the ones that enclose the cluster centre. As adopted by Meneghetti et al. (2010a, 2011) we will define the Einstein radius  $\theta_{E,med}$  as the median distance from the centre of these points. To be compatible with other definitions (Redlich et al. 2012), for each system we also compute the effective Einstein radius  $\theta_{E,eqv}$ , defined as the radius of the circle enclosing the same area as central critical points. In Fig. 2 we show the correlation between the two different definitions of the Einstein radius for the total sample of 12,288 clusters with mass between  $10^{14} M_\odot/h$  and  $3.16 \times 10^{15} M_\odot/h$  at six different redshifts. From the figure we notice that the median Einstein radius definition better captures the presence asymmetry of the matter distribution towards the cluster centre since many points lie above the least-squares fit to the data:  $\theta_{E,med} = \theta_{E,eqv} - 0.3$ . To emphasize this point we have colored the points referring to more asymmetric clusters (presenting a convergence ellipticity within  $R_{2500}$  – the radius which encloses 2500 times the critical density of the universe –  $\epsilon_{\kappa,2500} > 0.7$ ) magenta while those referring to the more spherical ones (with  $\epsilon_{\kappa,2500} < 0.1$ ) are green. We also note that the sample by Meneghetti et al. (2011) possesses a larger scatter in the relation mainly because of the large number of asymmetrical objects presented in their sample of strong lensing selected clusters.

While the halo mass and the concentration are two derived quantities from the weak and strong lensing signals,

the size of the Einstein radius is more directly estimated from the position of multiple images of background sources. In the literature there are many clusters in which tens of multiple images have been identified, allowing a very good determination of the size of the strong lensing region (Broadhurst et al. 2005a,b; Zitrin et al. 2011).

In the MOKA code, all  $\gamma$  and  $\alpha$  are computed in Fourier space where derivatives are easily and efficiently calculated. The Fourier transform of the convergence  $\hat{\kappa}(\mathbf{l})$ , is:

$$\hat{\kappa}(\mathbf{l}) = \int_{\mathbb{R}^2} d^2\theta \kappa(\theta) \exp(i\mathbf{l} \cdot \theta). \quad (12)$$

This is computed on a map of  $1024 \times 1024$  pixels with a zero padding region of 512 pixels to avoid artificial boundary effects. For each system, from the potential and the convergence maps, we compute the ellipticity  $\epsilon_{\Phi,500}$  of the potential and of the convergence  $\epsilon_{\kappa,500}$  at  $R_{500}$ , at the distance where the enclosed density drops below 500 times the critical value. We are interested in the potential ellipticity since  $\epsilon_{\Phi,500}$  is a quantity that can be directly compared with the X-ray morphology of observed galaxy clusters: systems that possess a regular and smooth X-ray map tend to have a small value of  $\epsilon_{\Phi,500}$ .

Combining the convergence and shear maps, for each MOKA cluster, we compute the reduced tangential shear profile and the error associated to each radial bin as follows. We assume a background density of sources of  $n_g = 30$  gal/arcmin<sup>2</sup> (which is a reasonable number for current and future space-based observations; see also the ESA mission EUCLID (Laureijs et al. 2011)), and locate on the map  $N_g = n_g \times A_{map}$  random points, where  $A_{map}$  represents the area of the map. We measure the reduced tangential shear at each of these  $N_g$  points and build a logarithmically azimuthally averaged profile from 0.01 Mpc/h up to the virial radius with bins equispaced by  $d \log(r) = 0.05$ . This ensures a good  $S/N$  in each bin both for low and high-redshift clusters. To each radial bin we assign an error given by the sum of two components:

$$\sigma_{g_+}^2 = \sigma_{\text{int}}^2 + \sigma_{g,\epsilon}^2, \quad (13)$$

where  $\sigma_{\text{int}}$  represents the rms of the measured reduced tangential shear from the map, and  $\sigma_{g,\epsilon}$  is the intrinsic shape of the background galaxies, that depends on the considered number density of the sources and on the intrinsic scatter in the ellipticity  $\sigma_\epsilon = 0.3$  (Hoekstra 2003; Hoekstra et al. 2013):

$$\sigma_{g,\epsilon}^2 = \frac{\sigma_\epsilon^2}{\pi(\theta_2^2 - \theta_1^2)n_g}; \quad (14)$$

here  $\theta_1$  and  $\theta_2$  the two extrema of the bin. The intrinsic scatter of the ellipticity of the background galaxies provides a noise that limits the accuracy of the shear measurements (Hoekstra 2003; Hirata & Seljak 2004). We recall that in our analysis we did not consider any uncertainty on the photometric redshift which would dilute the weak lensing signal.

An example is shown in Fig. 3 where the red circle with the error bars shows the average reduced tangential shear profile measured for a cluster at redshift  $z = 0.288$  with sources located at redshift  $z_s = 2$ ; the vertical line represents the median distance of the critical points from the cluster centre. The average of the reduced tangential shear in each annulus is calculated by averaging the corresponding values.

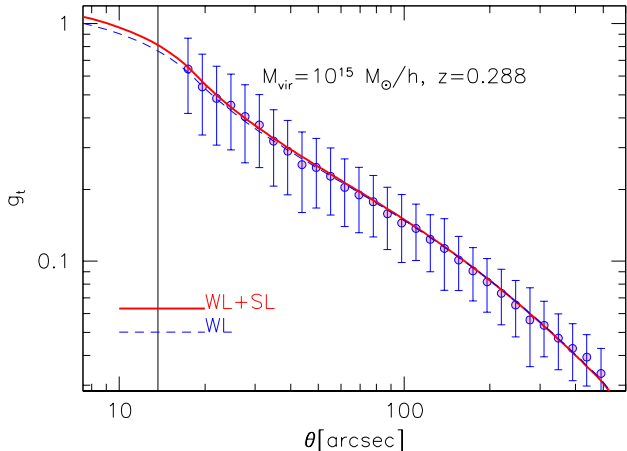


**Figure 3.** The reduced tangential shear profile of a galaxy cluster at redshift  $z = 0.288$  with sources at redshift  $z_s = 2$ . The error bars show the error associated to  $g_t$ , as in equation (13). The vertical line defines the size of the Einstein radius of the cluster. The solid line represents the best fit NFW profile obtained by taking into account both weak and strong lensing data, while the dashed one is the best fit when only the reduced tangential shear profile is considered.

Here we prefer not to use the weighted average, as done by Umetsu et al. (2011), because we assume the variance for the shear estimate to be zero since the value of  $g_+$  is directly computed using the corresponding map. To compute the spherical averaged profile we take the centre of the cluster to be the position of the BCG. In fact the location of the BCG can sometime be offset from the mass centroid of the corresponding matter density distribution (Oguri et al. 2010; Oguri & Takada 2011). However, in analyzing the strong lensing mass model of five clusters, Umetsu et al. (2011) find only a small offset (of the order of 20 kpc/h) between the BCG and the centre of mass.

For each cluster, we estimate the weak-lensing (WL) mass  $M_{est}$  and concentration  $c_{est}$  using an NFW profile fit to the reduced tangential shear profile by minimizing the quantity:

$$\chi_{WL}^2(M, c) = \sum_{i=1}^N \frac{[g_{NFW}(\theta_i | M, c) - g_t(\theta_i)]^2}{\sigma_{g_+,i}^2}, \quad (15)$$

where the index  $i$  runs on the number of bins and  $g_{NFW}(\theta_i)$  is computed using the relations for the convergence and the shear valid for a NFW halo (Bartelmann 1996). In Fig. 3, the dashed blue curve represents the best fit to the reduced tangential shear profile.

The information about the Einstein radius of the cluster allows also to define a strong lensing constraint (Sereni & Zitrin 2012; Zitrin et al. 2011). For a spherical NFW halo we use analytic formula for the convergence and the shear (Bartelmann 1996) and compute from equation (10) the corresponding Einstein radius given a certain mass and concentration. For the strong lensing constraint on the mass and concentration estimates we minimize the following quantity:

$$\chi_{SL}^2(M, c) = \frac{[\theta_E - \theta_{E,NFW}(M, c)]^2}{\sigma_E^2}; \quad (16)$$

we assume  $\sigma_E = 1$  arcsec (Jullo et al. 2010; Zitrin et al.

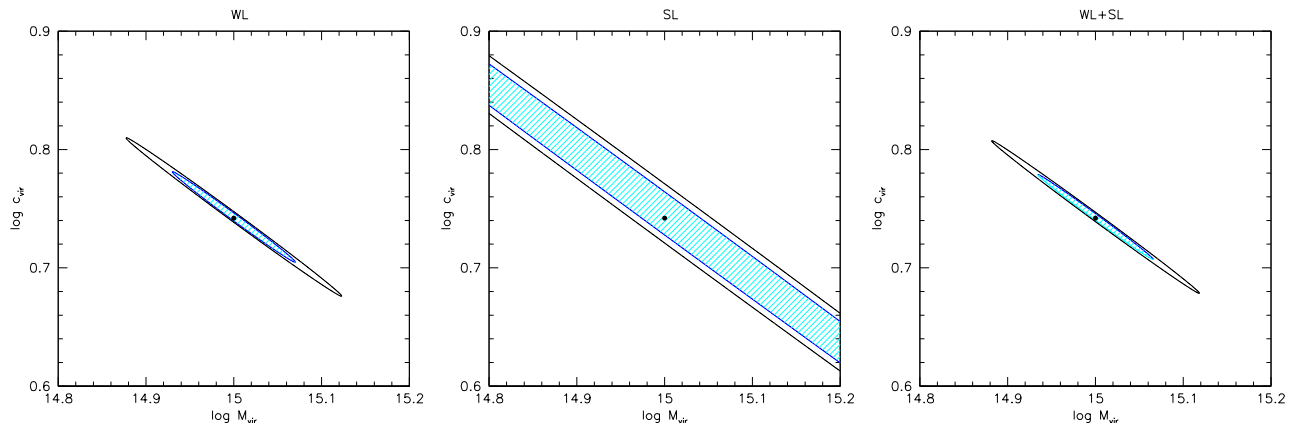


**Figure 4.** Weak lensing (left), strong lensing (centre) and weak+strong lensing (right) constraints estimating mass and concentration for a smooth, spherical NFW halo. The black dot represents the input halo mass and concentration. In all three cases the minimum of the  $\chi^2$  corresponds with the black dot.

2011,c; Host 2012) which represents the measurements error associated with the number of multiple images and from the positions of tangentially distorted galaxies available to reconstruct the critical curve of the cluster. In this approach we are comparing the measured size of the Einstein radius of the cluster with a spherical symmetric model. It is worth to notice that with this method we tend to overestimate the mass, since real clusters are triaxial and present substructures – so they are not axially symmetric. As described by Bartelmann (1995), a smaller and more realistic mass could be obtained modeling the strong lensing with a triaxial shape. In Fig. 3 the solid red curve represents the tangential shear profile of the cluster where mass and concentration have been estimated minimizing the combined WL and SL:  $\chi^2 = \chi_{WL}^2 + \eta\chi_{SL}^2$ . The parameter  $\eta$  is an integer ( $1 \leq \eta < N$ ) equal to the bins of  $g_+$  containing the value of the Einstein radius  $\theta_E$ . This ensures that when combining weak and strong lensing  $\chi^2$  we are putting together the same information, taking into account that the shear profile represents a differential quantity of the cluster matter distribution, while the size of the Einstein radius is a cumulative quantity since it is related to the total enclosed mass (Narayan & Bartelmann 1996; Bartelmann 2010) (for the case presented in Fig. 3 we have  $\eta = 1$ ). We recall the reader that even if we are using only the Einstein radius as strong lensing constraint we will label it as SL in all the figures.

In Fig. 4, we show the constraints obtained when recovering mass and concentration for the reference case of a smooth, spherical NFW halo. The left, center and right panels show weak, strong and weak+strong lensing constraints, respectively. In all the panels the black dot represents the mass and the concentration of the input halo which corresponds in all cases to the location of the minimum of the corresponding  $\chi^2$ .

### 3 MASSES AND CONCENTRATIONS FROM NFW FITTING

In this section we will present the results on the mass and the concentration estimates obtained from the whole con-

structed MOKA cluster sample. Since average halo structural properties depends on mass and redshift we will study how the mass and concentration bias depends on these quantities.

In Fig. 5 we show the average rescaled estimated mass as a function of the cluster mass for three of the six considered redshifts. The results of the three redshifts not displayed are consistent with those here presented. The rescaled mass is the ratio between the estimated and the true (3D) cluster mass (see Appendix A for the comparison between the true and 2D cluster masses). We recall that the simulations of the MOKA clusters include the presence of a BCG, the adiabatic contraction (ADC) of the dark matter component, triaxiality and subhaloes. Filled circles and triangles show the masses estimated considering SL+WL and WL alone, respectively; the shaded region encloses the  $1\sigma$  scatter of the distribution. From the figure we notice that for groups and small clusters the mass is typically underestimated by about 15%, for massive clusters the mass has a bias ranging from 5% down to a few percent, consistently with what has been found by Becker & Kravtsov (2011); Meneghetti et al. (2010b); Rasia et al. (2012). The higher bias in the mass estimate for the smallest systems is due to the triaxiality model by Jing & Suto (2002) implemented in MOKA and extended down to these masses. In this model, typically smaller systems tend to be more prolate than the more massive ones in agreement with the fact that they are more stretched by the gravitational field of the surrounding matter density distribution during their collapse (Sheth et al. 2001). The small trend of the normalization of the relation  $M_{est}/M_{vir} - M_{vir}$  as a function of redshift reflects the fact that MOKA clusters at higher redshifts tend on average to possess more substructures (van den Bosch et al. 2005; Giocoli et al. 2010a) and to have a larger 3D ellipticity  $\epsilon$  (Shaw et al. 2006, 2007; Giocoli et al. 2010a; Despali et al. 2013; Limousin et al. 2013). From the figure we notice that when the constraint on the size of the Einstein radius is included in the mass estimate the corresponding mass bias tends to be reduced: the modeling of the Einstein radius size is done using a spherical model and so on average we tend to measure a higher mass with the SL constrain (Bartelmann & Steinmetz 1996b). The absence of difference in the rescaled estimated

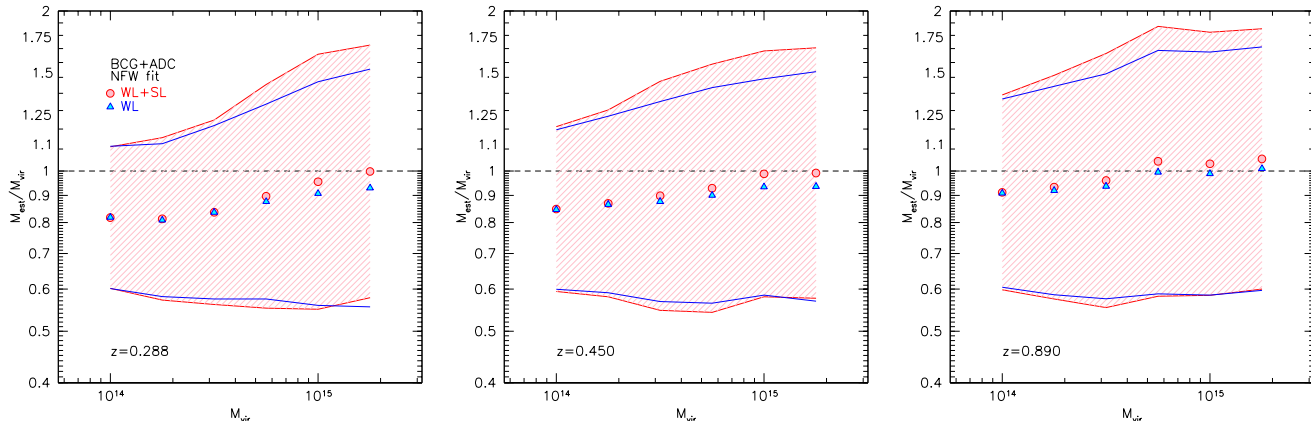


**Figure 5.** Average of the rescaled estimated mass as a function of the true cluster mass. We show the case in which the mass is estimated using WL+SL (circles) and only WL (triangles) information for systems at three different redshifts. The upper and lower curves show the  $1\sigma$  scatter of the corresponding distributions, red for WL+SL and blue for WL only. Each mass bin contains 2048 cluster realizations.

mass between WL and WL+SL for the smallest mass bins is due to the fact that most of those clusters are not strong lenses or have small Einstein radii: in those cases  $\chi^2_{SL}$  has a negligible contribution on the total  $\chi^2$ . Meneghetti et al. (2010b) perform a similar analysis. They study the lensing signals of three projections of three clusters extracted from a numerical simulation. In particular, in the left panel of their Fig. 16 they show the ratio between the estimated and true 3D mass obtained best fitting the reduced tangential shear profile of each cluster using, as we have done, an NFW functional. For the case  $M_{200}$ , the authors find a negative bias of about 15% – 5%, consistent with what we have found in this work. However, the flexibility and the speed of our algorithm MOKA allow us to generate and analyze a sample of clusters which is more than five orders of magnitude larger than the one studied by Meneghetti et al. (2010b).

We have also investigated what effect the cluster ellipticity on the plane of the sky have on the estimated mass. For each mass bin we have computed the median potential ellipticity  $\epsilon_{\Phi,500}$  – measured within  $R_{500}$  – and divided the halo sample into haloes with smaller or higher ellipticity. In Fig. 6 we present the average estimated mass as a function of the cluster mass for these two samples, considering only the clusters at redshift  $z = 0.288$ . The results for the other redshifts are quantitatively consistent. From the figure we see that the orientation of the main halo ellipsoid is an important source of bias in the measured halo mass, as already discussed by Meneghetti et al. (2010b). We consider in this case the situation in which mass and concentration have been estimated from the WL+SL constraints. Typically we see that for clusters whose major axis is oriented along the line of sight the mass tends to be overestimated – that are more spherical in the plane of the sky (Morandi et al. 2010), while the opposite occurs for clusters elongated in perpendicular direction: most spherical clusters are less biased than the most elliptical ones. An analogous result is presented in Meneghetti et al. (2010b) (see their fig. 17), where the cluster masses tend to be under (over)-estimated when large (small) angles between the line-of-sight and the major axis of the halo ellipsoid are present.

In Fig. 7, we show the average ratio between the esti-

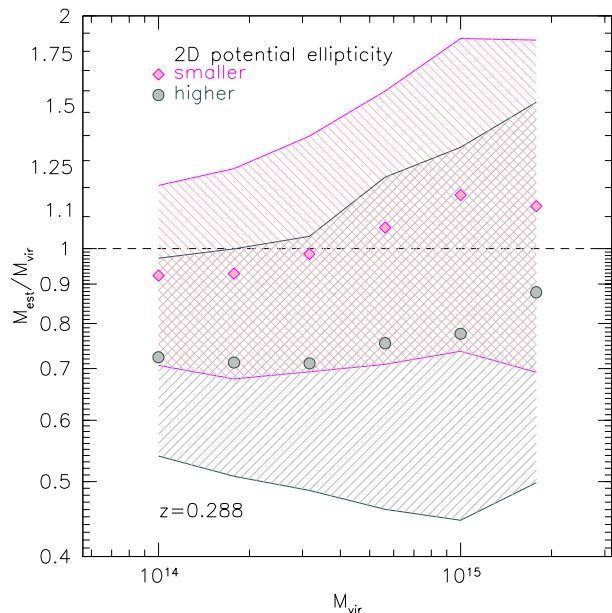


**Figure 6.** Average of the rescaled estimated mass as a function of the true cluster mass for haloes with higher or smaller ellipticity the plane of the sky at redshift  $z = 0.288$ . Masses and concentrations have been evaluated using both weak and strong lensing constraints.

mated concentration and the true one as a function of the cluster mass. The different panels refer to different redshifts and the data points have the same meaning as in Fig. 5. The results show that adding to the fit the constraint on the size of the Einstein radius does not change significantly the average value of the distribution, while it reduces the scatter for the most massive systems. The different panels show the presence of a positive bias for the smallest systems by less than  $\sim 10\%$ , which decreases with the lens redshift.

Our cluster lensing simulations include the presence of a BCG and a recipe for the adiabatic contraction. To understand how much these ingredients affect our mass and concentration measurements, we present in the left (right) panel

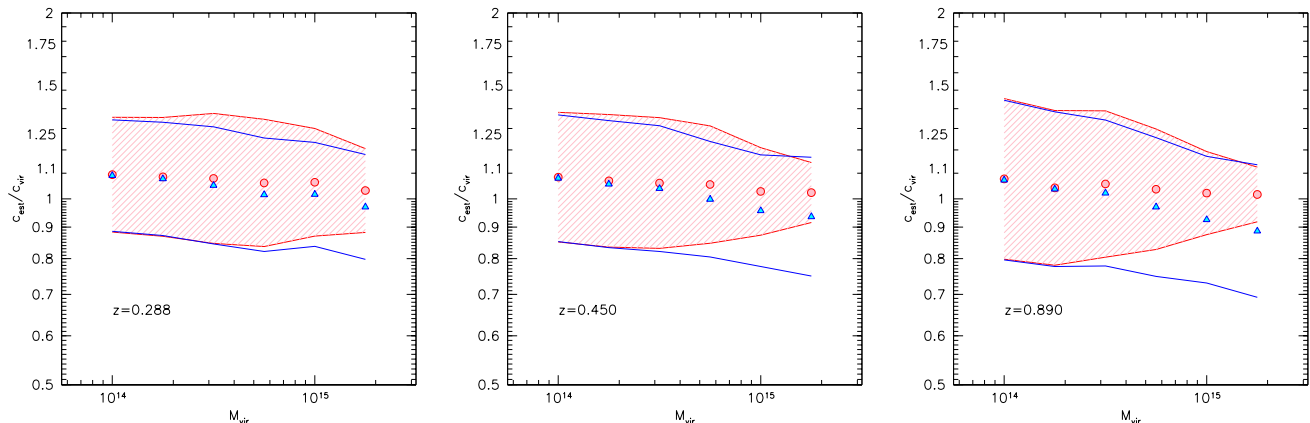


**Figure 7.** Average of the rescaled estimated concentration as a function of the true cluster mass. We show the case in which the concentration is estimated using WL+SL (red circles) and only WL (blue triangles) information for systems at three different redshifts. For each considered case, the corresponding upper and lower curves enclose the  $1\sigma$  scatter of the distribution at fixed mass.

of Fig. 8 the ratio between the mass (concentration) derived in simulations including BCG and ADC and that estimated in simulations without the central galaxy. Blue triangles and red circles refer to the case where only WL or WL+SL constraints are considered, respectively. We recall that in the first case holds  $M_{\text{vir}} = M_{\text{smooth}} + M_{\text{in subs}} + M_{\text{BCG}}$  while for the second  $M_{\text{vir}} = M'_{\text{smooth}} + M_{\text{in subs}}$ . We notice that fitting the whole profile with an NFW function we have an underestimate of the mass by only few percent with respect to the case in which the BCG is not present. The trend is different for the concentration which for small systems, where the cold baryon contribution is more important since star formation is fractionally more efficient in low-mass objects it is overestimated by 10 – 15%, while for the more massive clusters it is only few percent. The two data points refer again to the cases in which the fit is performed considering SL+WL (circles) and WL only (triangles). The shaded region encloses the  $1\sigma$  scatter of the distribution for a fixed value of the true cluster mass.

#### 4 MASSES AND CONCENTRATIONS FROM GENERALIZED NFW FITTING

Many studies analyzing haloes from DM-only numerical simulations have shown that the halo density profile (Neto et al. 2007; Gao et al. 2012) is well described by the NFW relation. However, in our case, we need to take into account the fact that real galaxy clusters are not only made up by dark matter – that accounts for more than 85% of the total mass – but also by baryons, divided into cold and hot components. While the hot component is more evenly spread in the potential well of the cluster – possessing a scale radius of the density profile  $r_{s,h}$  of the order of hundreds kpc/h – the cold component, that turns into the presence of a bright central galaxy, is more concentrated toward the center with a scale radius  $r_{s,c}$  much smaller than  $r_{s,h}$ . This translates into a total density profile which is different from an NFW relation and typically has an inner slope larger than unity. In order to better model the increase of the density distribution towards the cluster centre we can introduce a free parameter  $\beta$  in the NFW equation which allows the central

slope to freely vary (Zhao 1996; Jing 2000):

$$\rho_{gNFW}(r, \beta | M_{\text{vir}}, c_{\text{vir}}) = \frac{\rho_s}{(r/r_s)^\beta (1 + r/r_s)^{3-\beta}}, \quad (17)$$

where  $\rho_s$  represents the density within the scale radius  $r_s$ . In order to define the concentration it is useful to introduce the quantity  $r_{-2}$  as the radius at which the logarithmic density profile is  $-2$ . This allows us to write  $r_{-2} = (2 - \beta)r_s$  and the concentration  $c_{-2} \equiv R_{\text{vir}}/r_{-2} = c_{\text{vir}}/(2 - \beta)$ . The profile and the corresponding definitions match the NFW function when  $\beta = 1$ . The generalized NFW convergence can be obtained by integrating the profile in equation (17) along the line of sight:

$$\kappa_{gNFW}(r') = \int_{-\infty}^{\infty} \rho_{gNFW}(r, \zeta) d\zeta, \quad (18)$$

with  $r^2 \rightarrow r'^2 + \zeta^2$  and  $r'$  the radius vector on the plane of the sky. We can now define the dimensionless mass  $m(x) = \int_0^x x\kappa(x)dx$  and the shear:

$$\gamma_{gNFW}(x) = \frac{m_{gNFW}(x)}{x^2} - \kappa_{gNFW}(x), \quad (19)$$

with  $x = r/r_s$ . By setting  $\lambda_t = 0$  in equation (10), we can find the Einstein radius for the generalized NFW profile, that we use as reference model in constructing  $\chi^2_{SL}$ . The  $\chi^2$  is in this case minimized in order to obtain three parameters: the virial mass, the concentration and the inner slope  $\beta$  of the total density profile.

In Fig. 9, we show as a function of the halo mass the average rescaled mass and concentration, and the inner slope estimated by fitting the tangential shear profile and the size of the Einstein radius using a generalized NFW profile (the relations at the other redshifts are consistent with what presented here at  $z = 0.288$ ). The shaded region encloses the  $1\sigma$  scatter of the distributions at fixed halo mass, while the points represent the average value. From the figure we notice that using the gNFW profile the bias in the mass is reduced by about 10% for the smallest systems, but the scatter remains as large as in the NFW case. The average measure of the concentration is almost unbiased – of the order of few percent. From the right panel we notice that on average we tend to measure an inner slope larger than unity for the



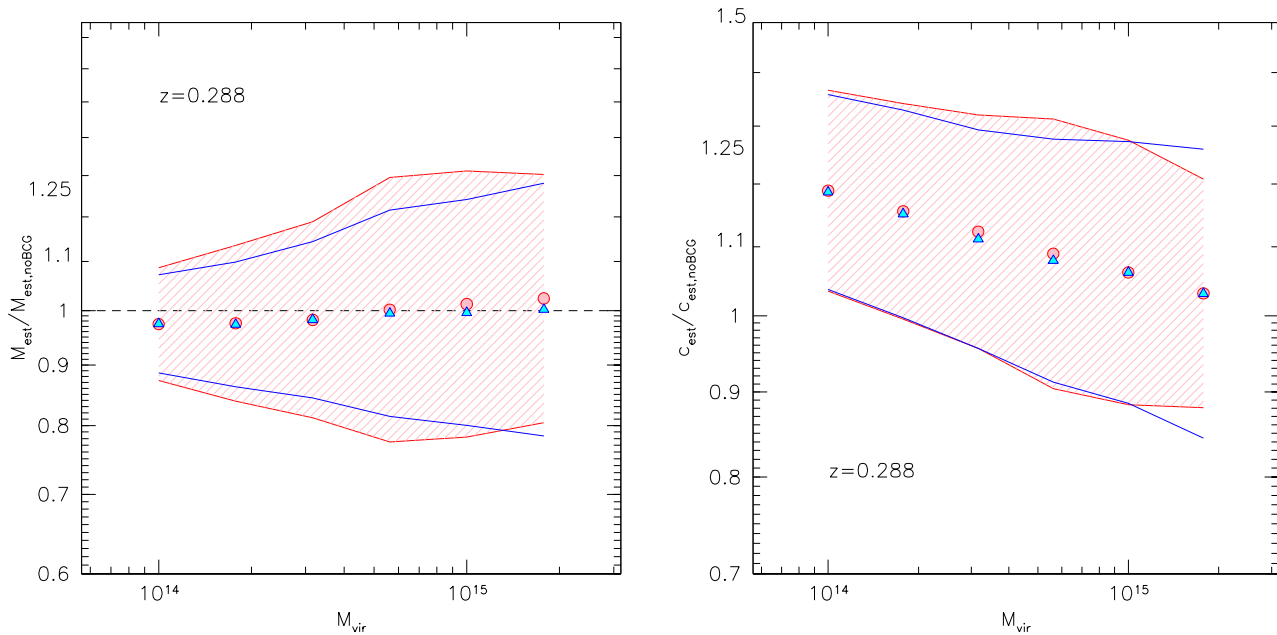


**Figure 8.** Ratio between different quantities estimated in simulations with BCG+ADC and without BCG as a function of the cluster mass. Left and right panels refer to mass and concentration, respectively. Blue triangles and red circles refer to the case where mass and concentration are estimated using only WL or WL+SL constrains, respectively.

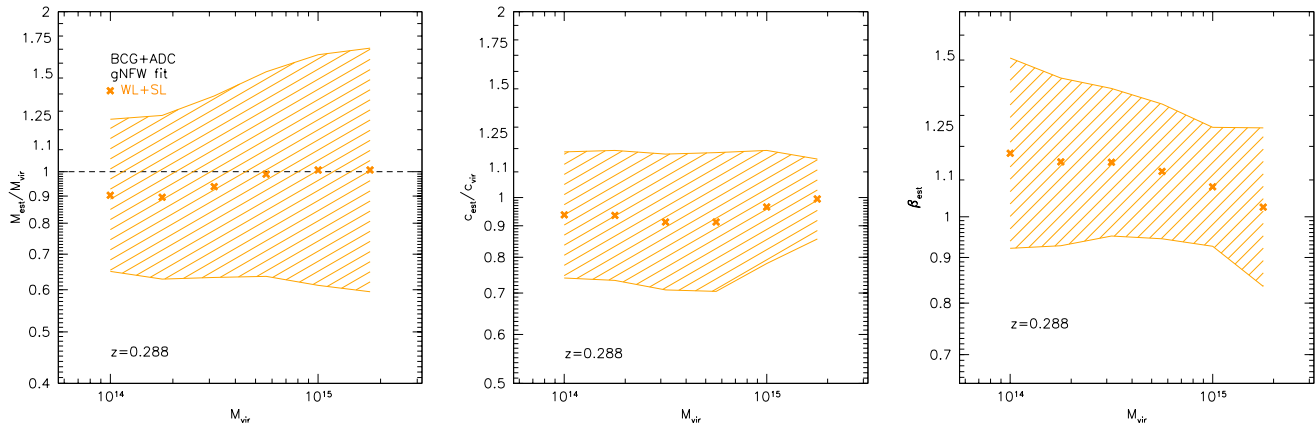


**Figure 9.** Average mass (left panel), concentration (center panel) and inner slope (right panel) estimated best fitting with the generalized NFW profile the reduced shear profile and the size of the Einstein radius, as a function of the cluster mass. The shaded region encloses the  $1\sigma$  scatter of the distribution.

smallest systems. This behavior is related to the fact that we are fitting the total 2D matter density distribution including the contribution both from DM and the bright central galaxy. Since the BCG steepens the profile and affects more significantly the core of the smallest systems, we tend to measure on average an inner slope that is even 20% larger than one. Even when the BCG is removed, a bias of 5 – 7% still remains for the smallest clusters due to the prolateness of their ellipsoids.

## 5 COSMOLOGICAL HALO SAMPLE

Until now many numerical simulations and analytical predictions have been developed to interpret the number of

collapsed objects and their concentration-mass relation at a given redshift. With the advent of the era of precision cosmology it is possible to use the halo mass function and the concentration-mass relation as an additional cosmological probe. Currently the relatively small number of available data combined with the bias and the scatter in estimated cluster properties limits the constraints on cosmological parameters. However, recently the Planck team (Planck Collaboration et al. 2013), using a sample of 189 galaxy clusters from the Planck SZ catalogue, was able to put good constraints on  $\Omega_m$  and  $\sigma_8$  the also emphasize the fact that the values of the cosmological parameters are degenerate with the hydrostatic mass bias and that the agreement between the cluster counts and the primordial CMB anisotropies can

be reached only assuming a mass bias of about 45%. However it is worth mentioning that the tension between the cosmological parameters ( $\Omega_m$  and  $\sigma_8$ ) derived from cluster counts and the ones derived from the Planck CMB temperature maps is alleviated when the SZ clusters are cross-correlated with the X-ray cluster maps from ROSAT (Hajian et al. 2013). At the same time the CLASH collaboration (Postman et al. 2012), reconstructing the mass distribution of a sample of 25 galaxy clusters using weak and strong lensing measurements, is exploring the possibility of eventually measuring deviations of the concentration-mass relation from the one measured in  $\Lambda$ CDM numerical simulations. However these works require precise knowledge of bias and scatter when comparing estimated and true cluster properties, like mass and concentration.

In this section, we will discuss how the mass and the concentration measured by fitting the tangential shear profile and constraining the size Einstein radius tend to modify the intrinsic concentration-mass relation for galaxy clusters. We will also discuss how selection effects on the cluster sample could modify the slope and the zero point of the relation.

As done previously, we consider the case of six different redshifts but with the halo sample extracted from the analytical Sheth & Tormen (1999) mass function. We consider haloes with a mass larger than  $10^{14} M_\odot/h$ . At each redshift, the number of haloes is created to match the number of collapsed objects present on the whole sky between  $z - \Delta z/2$  and  $z + \Delta z/2$  (with  $\Delta z = 0.01$ ). To increase the statistical sample, for each redshift we perform 8 different realizations.

We investigate the ellipticity distribution of these cosmological samples. In the left panel of Fig 10, we show the distribution of the 2D ellipticities, for each of the six redshifts considered. The parameters  $a$ ,  $b$  and  $c$  are the smallest, the intermediate and largest axes of the halo ellipsoid describing the dark matter halo, obtained from the Jing & Suto (2002) model. The corresponding 2D ellipticity distributions (on the plane of the sky with  $a'$  and  $b'$  representing the smallest and the longest axis of the ellipse) measured from the cluster convergence maps within  $R_{500}$  are shown in the right panel. It is interesting to notice the agreement with the results obtained by Meneghetti et al. (2010a) analyzing the clusters extracted from the MARENOSTRUM UNIVERSE simulation (Gottloeber et al. 2006; Gottlöber & Yepes 2007): our distributions lie in between with respect to the their measurements of the convergence ellipticity measured at  $R_{vir}$  and at  $0.1 \times R_{vir}$ . As expected from numerical simulations (Jing & Suto 2002; Despali et al. 2013) and also from analytic predictions of collapsing ellipsoids (Rossi et al. 2011), high-redshift clusters tend to be more elliptical, since more ongoing merging events make them typically unrelaxed. Notice that the higher ellipticities of high redshift clusters tend to enhance their strong lensing efficiency by stretching and increasing the critical area Zitrin et al. (2013a,b). In Appendix A we discuss the correlation between convergence and potential ellipticities comparing our finding with the model proposed by Golse & Kneib (2002).

### 5.1 The cluster mass function

As described previously in the paper, for each cluster we estimate the mass and the concentration in two ways. In the first case we use only the tangential shear profile (WL), while

**Table 1.** Least-squares fit to the estimated mass as a function of the true mass:  $\log M_{\text{set}}/M_{3D} = a \log M_{3D} + b$  ( $M_{3D}$  is in unit of  $M_\odot/h$ ). On the left for the case WL+SL, while on the right for the WL alone.

| redshift | a     | b      |  | a     | b      |
|----------|-------|--------|--|-------|--------|
| 0.187    | 0.062 | -0.970 |  | 0.045 | -0.731 |
| 0.288    | 0.077 | -1.179 |  | 0.051 | -0.811 |
| 0.352    | 0.073 | -1.121 |  | 0.046 | -0.727 |
| 0.450    | 0.059 | -0.905 |  | 0.037 | -0.597 |
| 0.548    | 0.059 | -0.900 |  | 0.040 | -0.627 |
| 0.890    | 0.055 | -0.813 |  | 0.040 | -0.608 |

in the second one we combine this with the measurement of the size of the Einstein radius adopting as a reference a NFW model (WL+SL); for the case WL+SL we perform the measurement also considering a generalized NFW model (gNFW WL+SL).

In Fig. 11, we show the cumulative all sky cluster mass function at three different redshifts. In each panel, the solid curve represents the analytical mass function of Sheth & Tormen (1999), while the black filled diamonds represent a catalogue extracted sampling this relation. Red filled circles and blue filled triangles show the mass function from weak and weak+strong lensing, respectively. In all panels the vertical line marks  $10^{14} M_\odot/h$ : the minimum mass of the extracted cluster sample. We notice that while for small masses the behavior is dominated by the difference between the true and the estimated mass, for large masses – since there are less haloes – it is dominated mainly by the scatter. We have tested this statement modifying the mass of the cosmological sample using the least-squares fit to the WL+SL masses performed to the data in Fig. 5, as expressed in Table 1, with a scatter  $\sigma_{\log M} = 0.25$  (open green squares points in the figure). From the bottom frame presented in each panel, where we show the difference of the measurements with respect to the analytical prediction, we notice the biased Gaussian sample matches quite well the WL+SL distribution up to the mass bin where the  $S/N = 5$  – we define the signal to noise for each bin as the ratio between the number of clusters and the corresponding Poisson error. The mass function obtained using a gNFW model as reference is similar to the others even if the mass bias is reduced in this case. This is due to the scatter still present in the rescaled estimated mass: the discrepancy with respect to the theoretical prediction is further reduced if  $\sigma_{\log M} = 0.1$ . If these deviations with respect to the theoretical mass function are not reduced, they will bias the estimated cosmological parameters in favor of models with higher  $\sigma_8$  and lower  $\Omega_m$ .

### 5.2 The concentration-mass relation

Biases and scatter of mass and concentration impact on the concentration-mass relation. In Fig. 12, we show the concentration-mass relation at three considered redshifts. The solid curve in each panel represents the  $c-M$  model by Zhao et al. (2009) at the corresponding redshift, while the black filled diamonds is the median intrinsic relation for the clusters obtained from this model assuming a log-normal scatter of 0.25. The blue filled triangles and the red filled circles show the median  $c-M$  relations obtained using WL

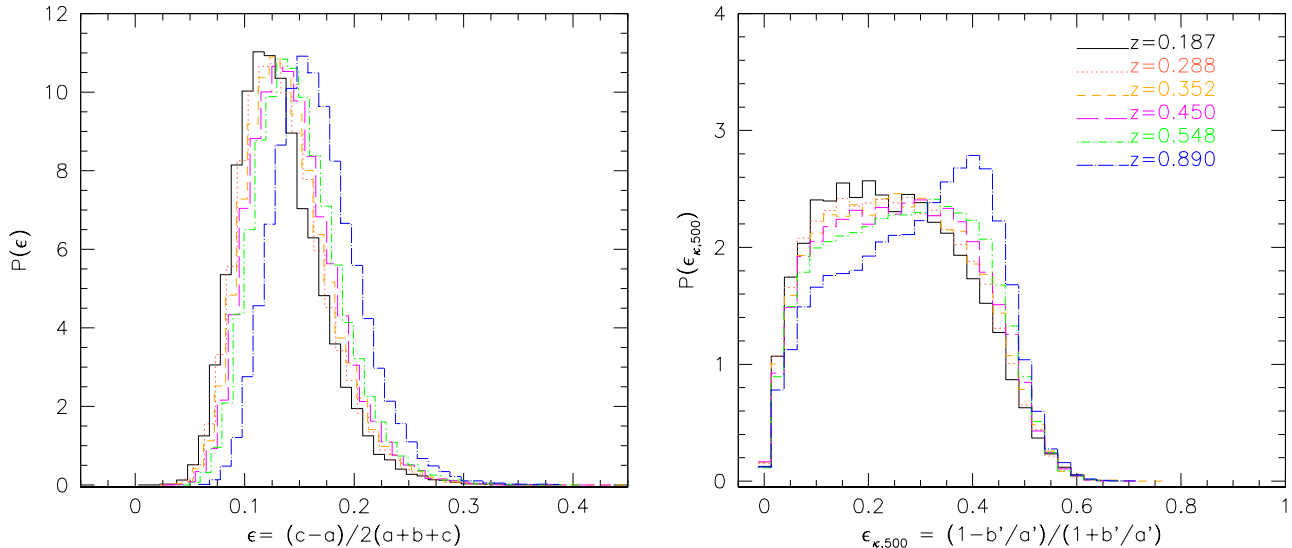


**Figure 10.** Left panel: intrinsic 3D ellipticity distribution of the main halo component for the samples of galaxy cluster at six different redshifts. Right panel: measured 2D ellipticity of the convergence at the radius at which the enclosed density reaches 500 times the critical value. Different line styles refer to the various considered redshifts, as labelled.

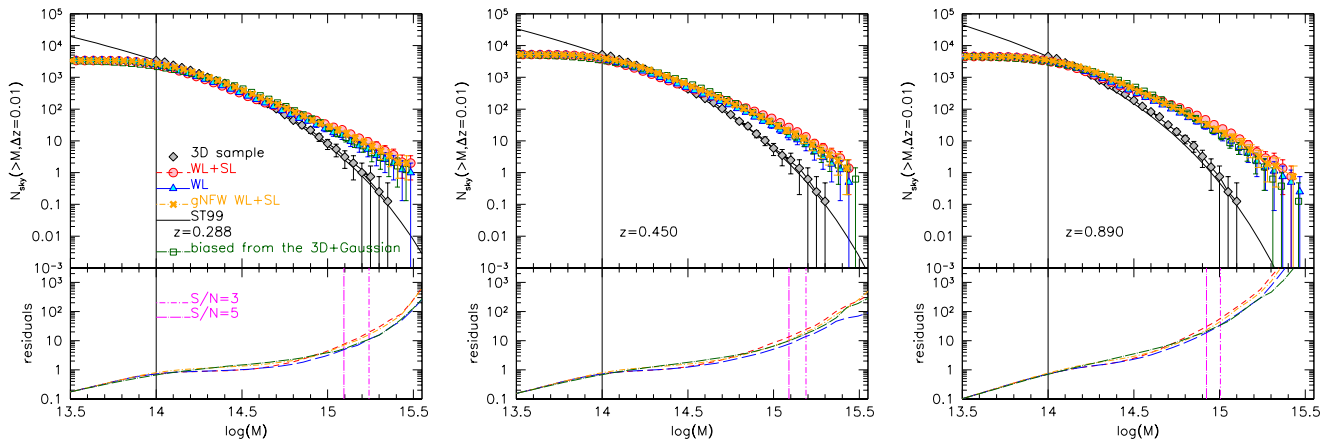


**Figure 11.** Cumulative all sky cluster mass functions at redshift  $z=0.288$  (left panel),  $z=0.450$  (central panel) and  $z=0.890$  (right panel). In each panel panel, the solid line in the top frame represents the analytical halo mass function (Sheth & Tormen 1999), while the black filled diamonds show the mass function of the cluster above  $10^{14} M_{\odot}/h$  obtained sampling this function. The filled blue triangles and the red filled circles represent the cluster mass function obtained using WL and WL+SL masses, respectively. For both cases, we have considered as a reference model a NFW halo. The orange cross show the WL+SL mass function, where a generalized NFW model has been used as a reference. The open green squares represent the mass function obtained biasing the halo mass of each cluster using the best fit relations reported in Table 1, and assuming a gaussian scatter of  $\sigma_{\log M} = 0.25$ . For all data the error bars represent their corresponding Poisson uncertainties. In each panel, the bottom frame represents the residuals as a function of the cluster mass of the WL, WL+SL and WL+SL using gNFW model with respect to the analytical Sheth & Tormen (1999) mass function.

and WL+SL estimates. In both cases, we notice that the concentration-mass relation for clusters tends to be overestimated by 20%. On average the difference with respect to the intrinsic  $c - M$  relation is reduced using gNFW masses and concentrations (orange crosses) and the median points are on average well inside the two central quartiles of the intrinsic distribution. For each data, the curves with the corresponding color enclose the first and the third quartiles of the distribution at fixed halo mass. From the figure we notice that describing the mass distribution as a triaxial ellipsoid tends to increase the normalization of the concentration-mass relation (Comerford & Natarajan 2007). As discussed

by Oguri et al. (2005) in the analysis of A1689, this may eventually reduce the apparent discrepancy between theory and observations.

Different observational campaigns (Okabe et al. 2010b; Postman et al. 2012) are trying to use the concentration-mass relation to test the agreements of observations with the predictions of structure formation in a  $\Lambda$ CDM cosmology. However it is reasonable to ask if the selection function of the observed clusters is important in reconstructing the  $c - M$  relation and, if so, how does it reflects, in both the true and reconstructed samples. For example it is interesting to point out the work by Sereno & Zitrin (2012), where

the  $c - M$  relation of the MACS cluster sample has been studied using strong lensing mass model reconstructions. This work first underlines the importance of triaxiality of the clusters when reconstructing their properties and second the selection function since high-redshift, unrelaxed clusters may form a different class of prominent strong gravitational lenses.

In order to understand how different selection functions change the  $c - M$  relation, in Fig. 13 we show the median relation for the cluster sample at redshift  $z = 0.288$  (the results at other redshifts are consistent with these) when the objects are selected to have different projected potential ellipticities,  $\epsilon_{\phi,500}$ . Selecting clusters in ellipticity implies also a selection in the shape of the X-ray emission: the ones with smaller ellipticity will also present a more spherical and relaxed X-ray morphology. Going from the left to the right panel, we show the  $c - M$  relations for clusters with  $\epsilon_{\phi,500} < 0.25$ ,  $\epsilon_{\phi,500} < 0.1$  and  $\epsilon_{\phi,500} < 0.05$ , respectively; the adopted symbols are the same as in Fig. 12. Looking at the filled black diamonds we notice that no particular bias appears in the intrinsic  $c - M$  relation, while the ones reconstructed using the concentrations and the masses derived from WL and WL+SL tends to move up for the more spherical systems. This behavior reflects the fact that, since haloes are in general prolate ellipsoids, the more spherical they are in the plane of the sky, the more elongated they must be along the line-of-sight – or they could be intrinsically spherical. So, even if the intrinsic  $c - M$  relations lie on the theoretical ones, the selection in ellipticity could introduce a bias in the estimated masses and concentrations. This effect is also seen in the  $c - M$  relation of clusters when their properties are estimated using a gNFW model as a reference: going from left to right, this is shown by the orange crosses, which tend to move toward higher values of concentration.

The effect is more drastic when we select clusters by their strong lensing features. In Fig. 14 we show the  $c - M$  relation selecting clusters to have an Einstein radius larger than 5, 12.5 and 20 arcsec, respectively. In this case, we notice again that the intrinsic  $c - M$  relation – showed by the black filled diamonds – tends to move up with respect to the solid curve, representing the reference model: intrinsically more concentrated haloes tend to be selected (Meneghetti et al. 2010a). Lensing reconstructed  $c - M$  relations are usually above the solid curve even by 20 – 30%. Selecting clusters by their strong lensing features not only picks up the ones that are more elongated along the line of sight but also the ones that are more elliptical in the plane of the sky (Zitrin et al. 2013b).

### 5.3 $c$ - $M$ relation for relaxed lenses

As a first case, we analyze the situation of building up the concentration-mass relation using a sample of relaxed clusters selected in a similar way to the CLASH sample. Since our cosmological cluster catalogues have been created for six discrete redshifts, we group the CLASH clusters in these bins. This corresponds to create six sub-samples, for the 25 clusters, with a temporal bin size of approximately 1 Gyr which is of the order of the cluster relaxing time. Each realization is constructed looping through the 25 clusters and then randomly selecting, from the corresponding catalogue,

**Table 2.** Least-squares fit to the samples WL+SL selected in potential ellipticity:  $\log c = a \log M + b$  ( $M$  is in unit of  $M_{\odot}/h$ )

| case              | a     | $\sigma_a$ | b    | $\sigma_b$ |
|-------------------|-------|------------|------|------------|
| all clusters      | -0.06 | 0.03       | 0.69 | 0.03       |
| $\theta_E > 5$    | -0.21 | 0.03       | 0.92 | 0.03       |
| $\theta_E > 12.5$ | -0.25 | 0.04       | 1.00 | 0.05       |
| $\theta_E > 20$   | -0.34 | 0.06       | 1.16 | 0.09       |

a cluster with a true mass of at least  $5 \times 10^{14} M_{\odot}/h$  and with a 2D ellipticity of the potential as in the Table 4 of Postman et al. (2012), when available. We repeat this procedure creating 10,000 different realizations of the CLASH-like sample. The ellipticity distribution of the sample nicely shows that the stronger the lens the larger is the elongation, and that the strongest lenses are very elongated either along the line of sight or in the lens plane.

In Fig. 15 we show the concentration-mass relation of these 10,000 realizations. For each cluster, we use the mass and the concentration estimated using a NFW model as reference combining weak and strong lensing constraints. In each panel the solid black curve shows the median of the sample and the gray region encloses the first and the third quartiles. The two external gray curves enclose 95% of the data. The different dashed curves show the theoretical concentration-mass relations at three redshifts. The four panels show: on the top left the case in which each sample does not contain any constrain on the minimum size of the Einstein radius, while in the other three the clusters are randomly selected with the condition of possessing an Einstein radius of at least 5, 12.5 and 20 arcsec, respectively. The  $c$ - $M$  relation built from the relaxed samples when no strong lensing selection is present is in very good agreement with the theoretical input models, while it increasingly steepens deviating from the theoretical expectations when a lower limit to the Einstein radius size is imposed. In Table 2 we present the slope and the zero point of the least-squares fit relation to the data, for each panel of the figure.

As a second case, in Fig. 16 we show the concentration-mass relation for 10,000 realizations of 28 MOKA clusters selected to match the sample by Oguri et al. (2012) as part of the Sloan Giant Arcs Survey (SGAS). In this case we have selected the clusters from our database to match the redshift, the ellipticity and the size of Einstein radius as listed in Tables 2 and 3 in Oguri et al. (2012). The red circles represent the median of the  $c - M$  relation for those clusters while the orange and pink lines enclose the quartiles and 95% of the data, respectively. The black line shows the least squares fit, that can be read as:

$$c_{vir} = 11.9 \pm 0.1 \left( \frac{M_{vir}}{10^{14}} \right)^{-0.37 \pm 0.02}. \quad (20)$$

The green triangles show the location of the SGAS-SDSS clusters in the figure when mass and concentration are estimated using both weak and strong lensing analyses, while the dotted line is the best fit relation (equation 26 from Oguri et al. (2012)). From the figure we notice that applying a realistic selection function to the simulated sample – in which multiple mass components, presence of the BCG and adiabatic contraction are considered – clarifies the tension

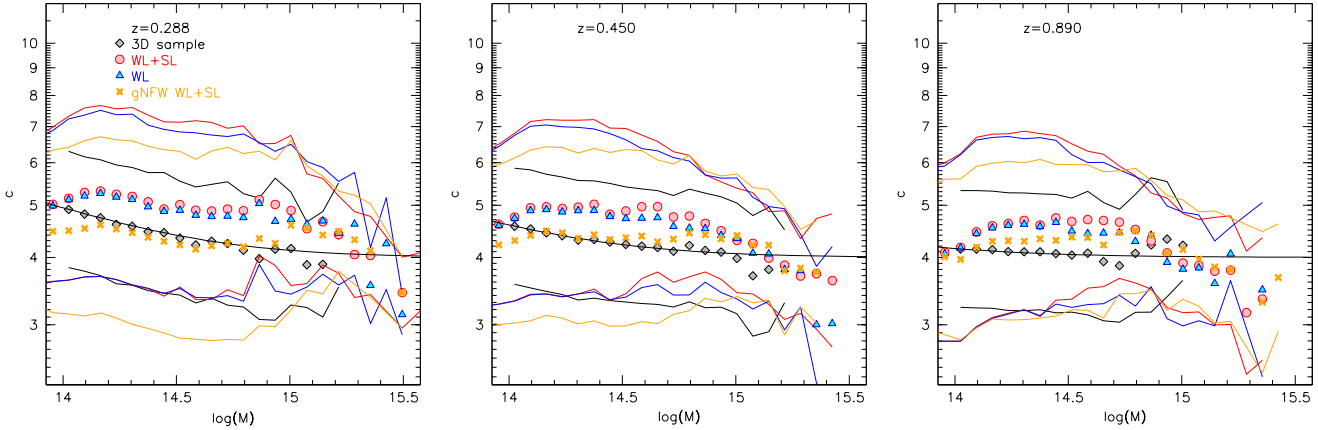


**Figure 12.** Concentration-mass relation at three different redshifts. In each panel the solid curve represents the Zhao et al. (2009) model, which we use as a reference when we assign the concentration to each halo. The black filled diamonds represent the intrinsic measured  $c - M$  relation, while the blue filled triangles and the red filled circles correspond to the  $c - M$  relations obtained for WL and WL+SL, respectively. The orange crosses show the relation for WL+SL when the mass and the concentration of the halo are obtained using the gNFW model as a reference. For each data, the curves with the same color enclose the first and the third quartiles of the distribution at fixed halo mass.

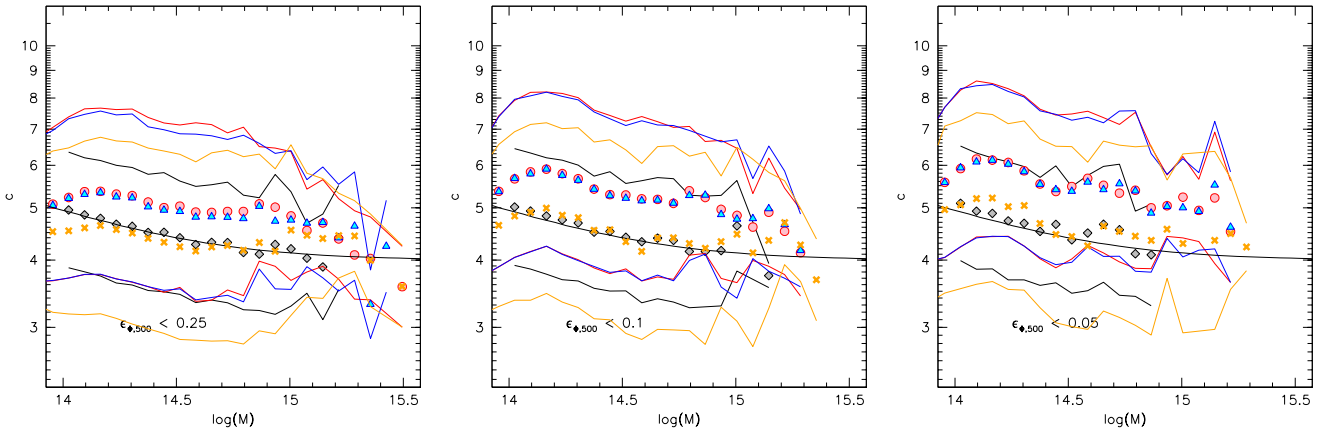


**Figure 13.** Same as Fig. 12 but for clusters selected with different limits in the potential ellipticity:  $\epsilon_{\phi,500} < 0.25$  (left panel),  $\epsilon_{\phi,500} < 0.1$  (central panel) and  $\epsilon_{\phi,500} < 0.05$  (right panel). The results refer to  $z = 0.288$  only.

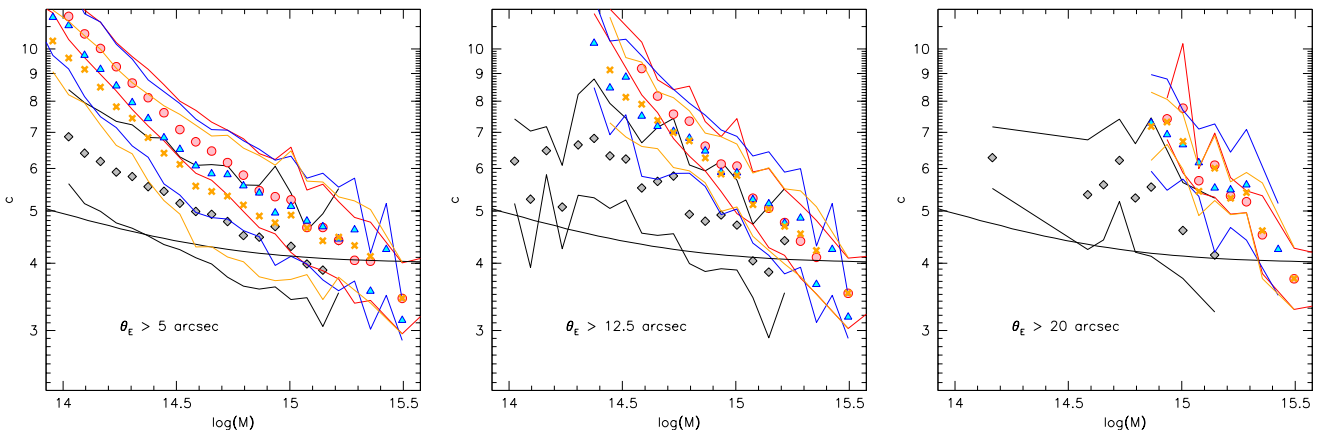


**Figure 14.** Same as Fig. 12 but for clusters selected with different limits in the size of the Einstein radius:  $\theta_E > 5$  (left panel),  $\theta_E > 12.5$  (central panel) and  $\theta_E > 20$  arcsec (right panel). Also in this case the results refer to  $z = 0.288$  only.

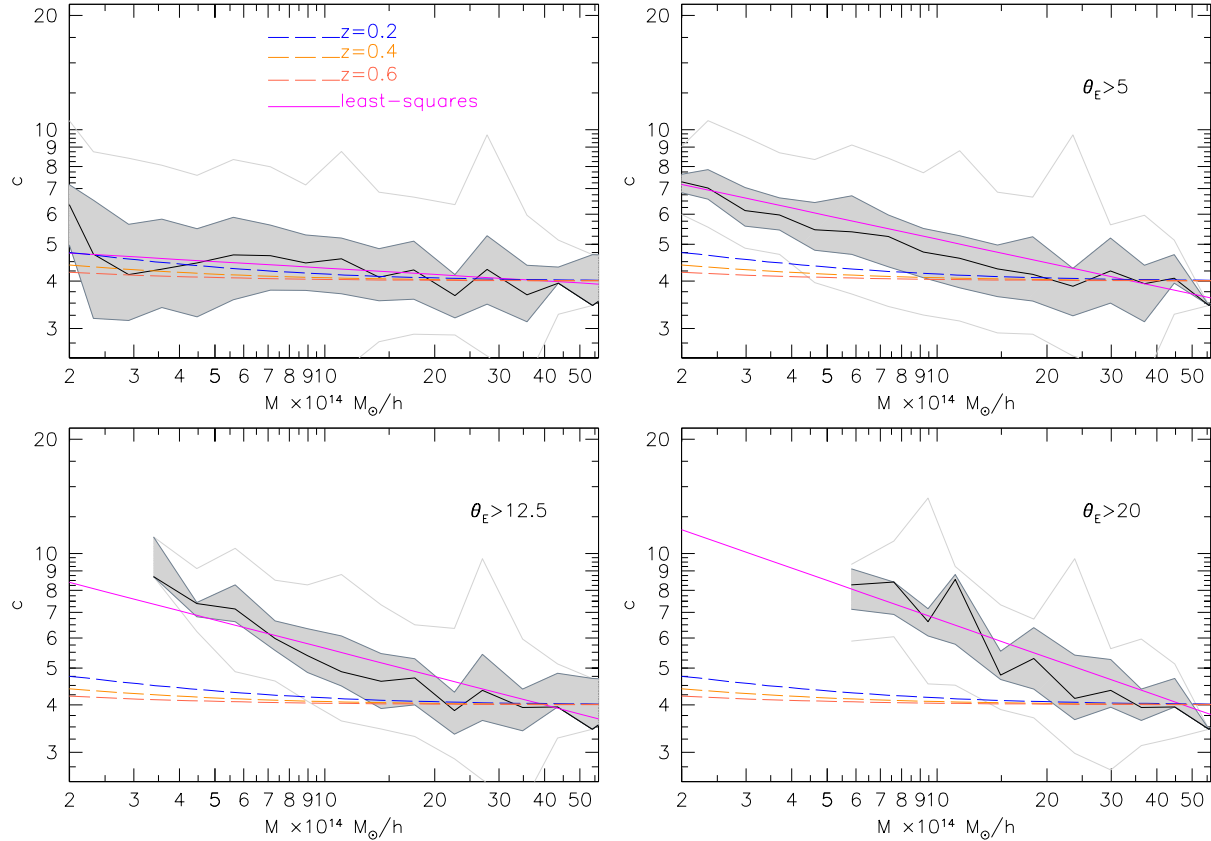


**Figure 15.** Median concentration-mass relation for 10,000 realizations of 25 clusters selected in potential ellipticity, where mass and concentration are estimated using WL+SL constraints considering an NFW profile as reference model. The shaded dark gray region encloses the first and the third quartiles of the distribution, while the gray curves are 95% of the data. The solid (magenta, for the colored version of the figure) represent the least-squares fit to the data.

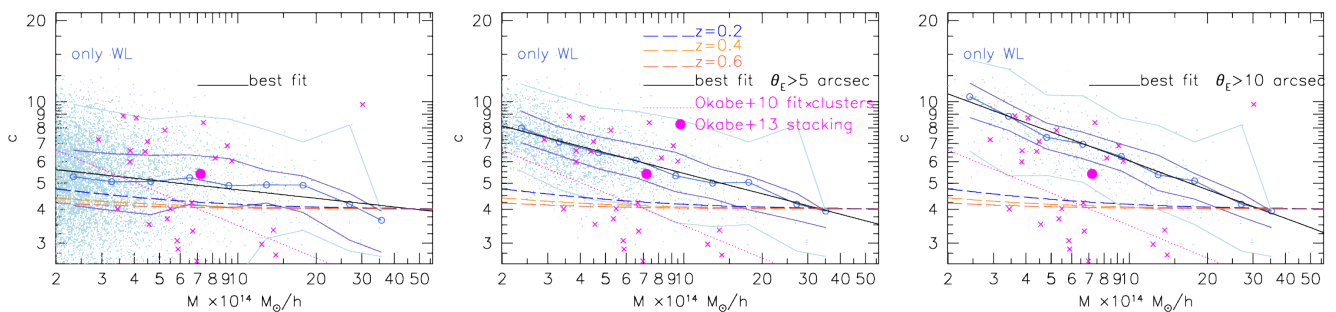


**Figure 17.** Median concentration-mass relation for 10,000 realizations of 26 clusters selected in redshift as the LoCuSS sample by Okabe et al. (2010b), where mass and concentration are measured using only WL data through the reduced tangential shear profile. In the left, central and right panel we show the relation obtained from our MOKA sample, considering all clusters, those with an Einstein radius larger than 5 arcsec and 10 arcsec, respectively. In each panel, the blue circles represent the median of the distribution, while the blue and the light-blue lines enclose the quartiles and 95% of the data, respectively.

between the  $c - M$  relation predicted in numerical simulations and the best-fit on the observed dataset.

As a last case, we compare our predictions to those obtained by analyzing the weak lensing data of 26 clusters from the LoCuSS survey, listed in Table 6 of Okabe et al. (2010b). In this case, to be consistent with their analysis, we have considered only the situation in which the mass and the concentration are estimated by fitting the reduced tangential shear profile. The MOKA sample has been selected from

our database to match the redshift of the LoCuSS clusters (see Table 1 by Okabe et al. (2010b)). In the left panel of Fig. 17, we show the median estimated concentration-mass relation obtained for 10,000 realizations of the sample. The solid black line represents the least-squares fit to our data. In the central panel we have considered only clusters with an Einstein radius larger than 5 arcsec, while in the right those with  $\theta_E > 10$  arcsec. In all panels the magenta crosses represent the location in the mass-concentration diagram

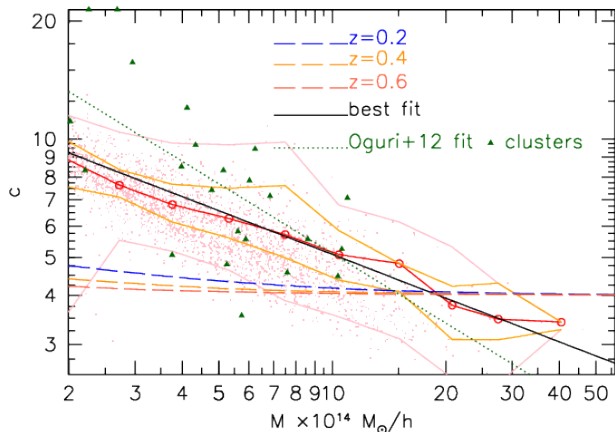


**Figure 16.** Median concentration-mass relation for 10,000 realizations of 28 clusters selected using the convergence ellipticity and the Einstein radius to match the sample of Oguri et al. (2012). The red circles show the median of the distribution while the orange and pink lines enclose the quartiles and 95% of the data points, respectively. The black solid line is the least-squares fit to the selected MOKA clusters. Dashed curves, as in Fig. 15, show the theoretical  $c - M$  predictions at the corresponding redshifts.

**Table 3.** Best fit parameters of the  $c - M$  for 10,000 realizations of the LoCuSS galaxy cluster sample:  $c_{vir} = c_N (M_{vir}/10^{14})^{-\alpha}$

|                 | $c_N$            | $\alpha$        |
|-----------------|------------------|-----------------|
| all clusters    | $6.03 \pm 0.08$  | $0.10 \pm 0.03$ |
| $\theta_E > 5$  | $9.69 \pm 0.05$  | $0.25 \pm 0.01$ |
| $\theta_E > 10$ | $13.68 \pm 0.08$ | $0.35 \pm 0.01$ |

of LoCuSS clusters and the filled circle the values obtained by performing a stacking analysis of them as described by Okabe et al. (2013). As already discussed, the strong lensing selection tends to increase both the normalization and the slope of the concentration-mass relation. In Table 3 we summarize the slope and the zero point of best fitting the recovered  $c - M$  relations for the three cases.

## 6 SUMMARY AND CONCLUSION

In this work we have studied how well galaxy cluster masses and concentrations are recovered using strong and weak lensing signals. Using an NFW halo model as reference, we recover mass and concentration using only weak lensing data or combining them with a measurement of the size of the Einstein radius. In addition, for the case in which we combine both WL and SL measurements we have made estimates of the mass and concentration using a generalized NFW model, which reduces both mass and concentration biases while introducing a new free parameter (the inner slope of the density profile). We summarize our study and main results as follows.

- On average, lensing analysis provides biases on the cluster mass that depend on the host halo mass. Small systems typically present a mass bias of about 15% while for the more massive ones the bias almost vanishes. The scatter has a log-normal distribution with a  $\sigma_{\log M} \approx 0.25$ . For the most

massive systems, adding the constraint on the size of the Einstein radius reduces the bias to a few percents.

- The estimated concentration is slightly positively biased and decreasing with the halo mass. This behavior can be attributed to the presence of the BCG at the center of the cluster and to the adiabatic contraction (here included unlike in the previous work (Giocoli et al. 2012c)).

- Adopting a generalized NFW model for fitting weak and strong lensing data reduces both mass and concentration biases. However, this introduces an additional free parameter, the inner slope of the density profile,  $\beta$ .

- The bias and the scatter in the estimated mass modify the shape of the mass function with respect to the theoretical prediction, from which the cosmological sample is drawn. However, for mass bins in which cluster count has a  $S/N \geq 5$  the residuals between the input and the recovered mass function are smaller by a factor of 5 – 7.

- The uncertainties on the cluster mass and concentration also change the mass-concentration relation. On average, when an NFW model is used to fit the clusters, the normalization of the recovered  $c - M$  relation has a normalization higher by 5 – 7%. The use of a generalized NFW helps to recover a  $c - M$  relation in better agreement with the theoretical expectations.

- The biases in the concentration-mass relation, as reported by the analyses of different galaxy cluster surveys, are clarified when selecting from our MOKA sample a relaxed sub-sample of systems.

To conclude, in this work we have presented a detailed and systematic analysis of the estimation of mass and concentration of clusters using lensing data (weak and weak+strong). We have studied how the mass and concentration biases depend on the halo mass and redshift. We have presented how the bias and the scatter in the estimated mass and concentration influence the halo mass function and the  $c - M$  relation. In particular, we have discussed how different selection criteria affect the concentration-mass relation and we have found that strong lens clusters may have a concentration as high as 20 – 30% above the average, at the fixed mass.

## ACKNOWLEDGEMENTS

CG and RBM’s research is part of the project GLENCO, funded under the European Seventh Framework Programme, Ideas, Grant Agreement n. 259349. We acknowledge financial contributions from contracts ASI/INAF I/023/12/0 and by the PRIN MIUR 2010-2011 “The dark Universe and the cosmic evolution of baryons: from current surveys to Euclid”. CG and LM also acknowledge the financial contribution by the PRIN INAF 2012 “The Universe in the box: multiscale simulations of cosmic structure”. SE acknowledges the financial contribution from contracts ASI/INAF I/088/06/0 and PRIN-INAF 2012. CG would like to thank Giuseppe Tormen and Vincenzo Mezzalana to have host part of the computer jobs run to produce the simulated galaxy cluster sample. Part of the simulations of this project have been run during the Class C Project-HP10CMXLBH (MOKALEN3) CG would like to particularly thank Matthias Bartelmann for useful and stimulating discussions. We are also grateful to Maruša Bradač Anja Von

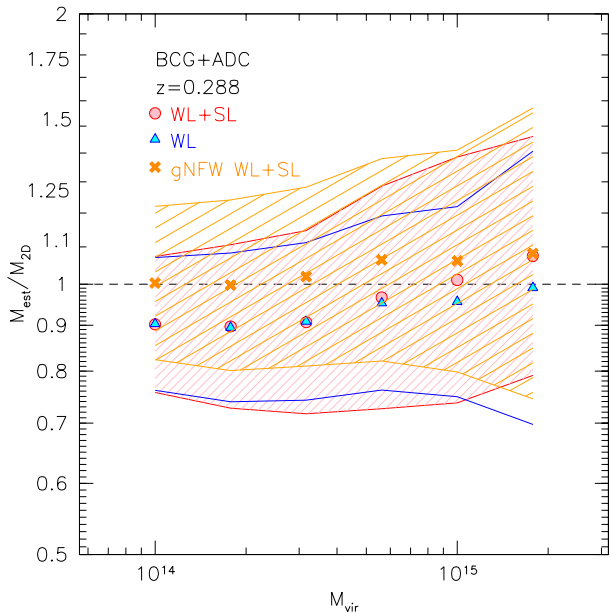


**Figure A1.** Average of the rescaled – with respect to the 2D mass – estimated mass as a function of the 2D cluster mass, for the systems at redshift  $z = 0.288$ . We show the case in which the mass is estimated using WL+SL (circles) and WL only (triangles) information using an NFW model as a reference when minimizing the total  $\chi^2$ . The upper and lower curves enclose the  $1\sigma$  scatter of the distribution. Each mass bin contains 2048 cluster realizations. The orange crosses show the same quantity when using gNFW model as a reference for both weak and strong lensing.

der Linden, Stefano Borgani, Stefano Andreon and Mauro Sereno for the conversations had during the conference in Madonna di Campiglio in March 2013. We are also grateful to the anonymous referee for his/her comments and suggestions that helped to improve the presentation of our results.

## APPENDIX A: 2D MASSES

The measurement of gravitational lensing gives an estimate of the projected mass which is causing the distortion of the shape of background galaxies and the creation of multiple images, without any assumption about the dynamical state of the system. However some assumption is needed when the mass reconstruction is deprojected from 2D to 3D.

In Fig. A1 we show the estimated mass derived from weak and weak + strong lensing rescaled with respect to the 2D one as a function of the true cluster mass for redshift  $z = 0.288$ . We do not show the results for different redshifts since they are extremely similar this case. From the figure, when we assume an NFW halo as a reference model, we notice that for smaller masses the bias with respect to the 2D mass is of about ten percent, while at larger masses it is almost negligible, well below 5 – 7%. One more interesting result is that the scatter is smaller than the one measured in the relation  $M_{\text{est}}/M_{3\text{D}}$ . The case WL+SL using generalized NFW model shows on average no particular bias for any cluster mass sample.

## APPENDIX B: CONVERGENCE AND POTENTIAL ELLIPTICITY

The flexibility of the MOKA code allows us to study the relationship between the convergence and the potential ellipticity. In order to do so we measure the ellipticity from convergence and lensing potential maps, both within  $R_{500}$ . In this context, we use the relation of Golse & Kneib (2002) to link  $\epsilon_\kappa$  and  $\epsilon_\phi$  for pseudo-elliptical NFW lens models. However, simulated and real clusters are different from a simple one-component model and we are interested in understanding if, and up to what point, their relation is valid for our MOKA cluster sample. At this aim, we consider two samples of clusters, one triaxial without BCG and satellite population and the second one containing them. The left panel of Fig. B1 shows the correlation between the potential and the convergence ellipticity for the first sample, when considering together all clusters at all redshifts. The filled circles represent the median at fixed  $\epsilon_{\kappa,500}$ , while the solid lines enclose the first and the third quartiles. In the bottom panel of the figure, we show the residuals of  $\epsilon_{\phi,500}$  with respect to  $\epsilon_{\phi,500,GK}$  that represents the ellipticity of the potential directly computed from  $\epsilon_{\kappa,500}$ , using the Golse & Kneib (2002) formalism.

In order to estimate  $\epsilon_{\phi,500,GK}$  we solve the equation:

$$\epsilon_{\kappa,500,GK} = a_1 \epsilon_{\phi,500} + a_2 \epsilon_{\phi,500}^2, \quad (\text{B1})$$

taken from Golse & Kneib (2002), where:

$$\begin{aligned} a_1 &= 3.31 + 0.280 x_{500} \\ a_2 &= -2.66 - 0.512 x_{500}, \end{aligned} \quad (\text{B2})$$

and  $x_{500} = R_{500}/r_s$ . We recall that this relation has been obtained by applying the formalism to a pseudo-elliptical NFW profile, for a limited range of the convergence ellipticity: typically  $\epsilon_\kappa \lesssim 0.4$ . We notice, that since our definition of 2D ellipticity differs from the one adopted by Golse & Kneib (2002), the parametrization of  $a_1$  and  $a_2$  differs by a constant factor of 0.64. From the bottom left panel we notice that the Golse & Kneib (2002) formalism perfectly captures the potential ellipticity from the convergence for  $\epsilon_{\kappa,500} < 0.5$  with a very small rms. The situation is different for the case in which we add BCG and substructures to the convergence map, see right panel of Fig. B1. In this case, we notice that on average the analytical prediction is still valid but the scatter of the correlation is much larger. Moreover the rms between the ellipticity measured in the potential map and the one inferred from the convergence ellipticity is larger than in the previous case by more than one order of magnitude.

## REFERENCES

- Applegate D. E., von der Linden A., Kelly P. L., Allen M. T., Allen S. W., Burchat P. R., Burke D. L., Ebeling H., Mantz A., Morris R. G., 2012, ArXiv e-prints  
 Bartelmann M., 1995, A&A, 299, 11  
 Bartelmann M., 1996, A&A, 313, 697  
 Bartelmann M., 2010, ArXiv e-prints  
 Bartelmann M., Schneider P., 2001, Physics Reports, 340, 291  
 Bartelmann M., Steinmetz M., 1996b, MNRAS, 283, 431



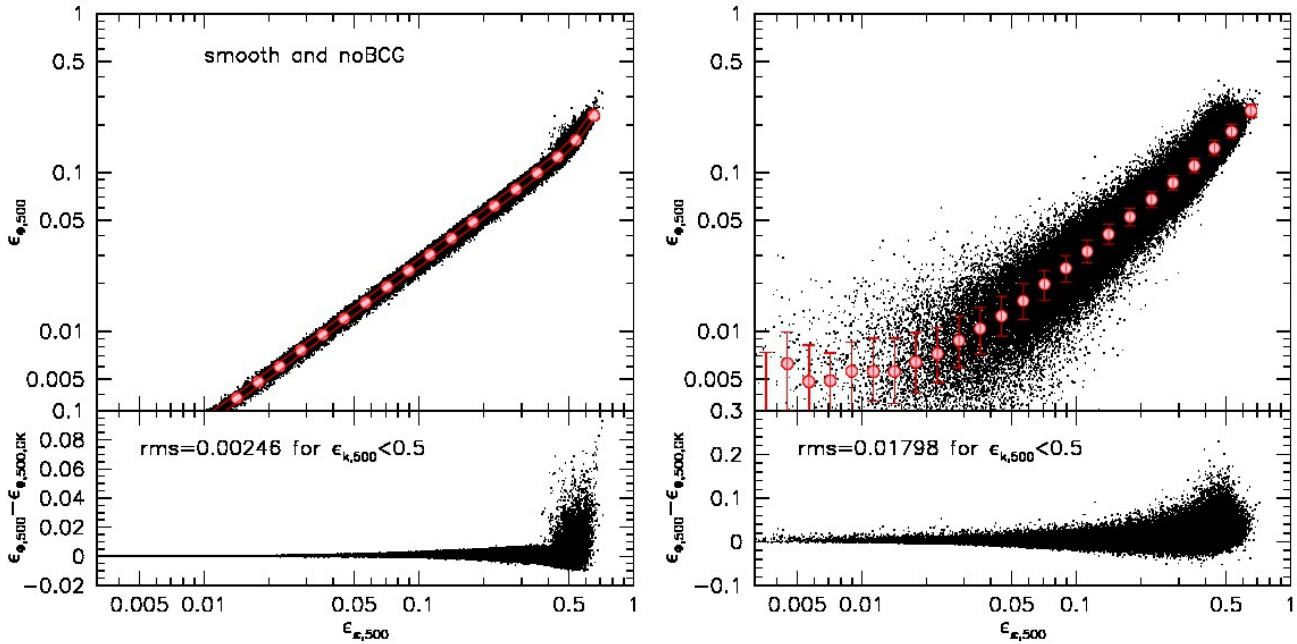


**Figure B1.** Potential vs convergence ellipticity correlation. The dots in both panel show halo by the halo correlation while the filled circles with the error bars correspond to the median and the quartiles of the distribution in bins of convergence ellipticity. Both the convergence and the potential ellipticities have been measured from the respective maps within  $R_{500}$ . In the left panel we show the correlation for smooth haloes without substructures and central galaxy. In the right panel we consider more realistic clusters where substructures and BCG are included. The bottom panels show the residuals of the measured potential ellipticity with respect to the one estimated from  $\epsilon_{k,500}$  using the Golse & Kneib (2002) relation (see equation (B1)).

- Becker M. R., Kravtsov A. V., 2011, *ApJ*, 740, 25
- Broadhurst T., Benítez N., Coe D., Sharon K., Zekser K., White R., Ford H., et al. B., 2005b, *ApJ*, 621, 53
- Broadhurst T., Takada M., Umetsu K., Kong X., Arimoto N., Chiba M., Futamase T., 2005a, *ApJ*, 619, L143
- Bryan G. L., Norman M. L., 1998, *ApJ*, 495, 80
- Coe D., Zitrin A., Carrasco M., Shu X., Zheng W., Postman M., Bradley L., Koekemoer et al. 2013, *ApJ*, 762, 32
- Comerford J. M., Natarajan P., 2007, *MNRAS*, 379, 190
- Despali G., Tormen G., Sheth R. K., 2013, *MNRAS*, 431, 1143
- Eke V. R., Cole S., Frenk C. S., 1996, *MNRAS*, 282, 263
- Ettori S., Donnarumma A., Pointecouteau E., Reiprich T. H., Giodini S., Lovisari L., Schmidt R. W., 2013, *Space Sci.Rev.*, 177, 119
- Ettori S., Gastaldello F., Leccardi A., Molendi S., Rossetti M., Buote D., Meneghetti M., 2010, *A&A*, 524, A68+
- Ettori S., Morandi A., Tozzi P., Balestra I., Borgani S., Rosati P., Lovisari L., Terenziani F., 2009, *A&A*, 501, 61
- Fasano G., Bettoni D., Ascaso B., Tormen G., Poggianti B. M., Valentinuzzi T., D’Onofrio M., Fritz J., Moretti A., Omizzolo A., Cava A., Moles M., Dressler A., Couch W. J., Kjærgaard P., Varela J., 2010, *MNRAS*, 404, 1490
- Fedeli C., 2012, *MNRAS*, 424, 1244
- Gao L., Navarro J. F., Frenk C. S., Jenkins A., Springel V., White S. D. M., 2012, *ArXiv e-prints*
- Giocoli C., Meneghetti M., Bartelmann M., Moscardini L., Boldrin M., 2012a, *MNRAS*, 421, 3343
- Giocoli C., Meneghetti M., Ettori S., Moscardini L., 2012c, *MNRAS*, 426, 1558
- Giocoli C., Tormen G., Sheth R. K., 2012b, *MNRAS*, 422, 185
- Giocoli C., Tormen G., Sheth R. K., van den Bosch F. C., 2010a, *MNRAS*, 404, 502
- Golse G., Kneib J.-P., 2002, *A&A*, 390, 821
- Gottlöber S., Yepes G., 2007, *ApJ*, 664, 117
- Gottloeber S., Yepes G., Wagner C., Sevilla R., 2006, *ArXiv Astrophysics e-prints*
- Hajian A., Battaglia N., Spergel D. N., Bond J. R., Pfrommer C., Sievers J. L., 2013, *JCAP*, 11, 64
- Hernquist L., 1990, *ApJ*, 356, 359
- Hirata C. M., Seljak U., 2004, *Phys.Rev.D*, 70, 063526
- Hoekstra H., 2003, *MNRAS*, 339, 1155
- Hoekstra H., Bartelmann M., Dahle H., Israel H., Limousin M., Meneghetti M., 2013, *Space Sci.Rev.*, 177, 75
- Host O., 2012, *MNRAS*, 420, L18
- Jaffe W., 1983, *MNRAS*, 202, 995
- Jing Y. P., 2000, *ApJ*, 535, 30
- Jing Y. P., Suto Y., 2002, *ApJ*, 574, 538
- Jullo E., Natarajan P., Kneib J.-P., D’Aloisio A., Limousin M., Richard J., Schimd C., 2010, *Science*, 329, 924
- Kazantzidis S., Bullock J. S., Zentner A. R., Kravtsov A. V., Moustakas L. A., 2008, *ApJ*, 688, 254
- Kazantzidis S., Kravtsov A. V., Zentner A. R., Allgood B., Nagai D., Moore B., 2004, *ApJ*, 611, L73
- Kazantzidis S., Zentner A. R., Kravtsov A. V., Bullock J. S., Debattista V. P., 2009, *ApJ*, 700, 1896
- Keeton C. R., 2001, *ApJ*, 561, 46
- Killedar M., Borgani S., Meneghetti M., Dolag K., Fabjan D., Tornatore L., 2012, *MNRAS*, 427, 533
- Kneib J.-P., Natarajan P., 2011, *A&A Rev.*, 19, 47
- Laureijs R., Amiaux J., Arduini S., Auguères J. ., Brinch-

- mann J., Cole R., Cropper M., Dabin C., Duvet L., et al. 2011, ArXiv e-prints
- Limousin M., Morandi A., Sereno M., Meneghetti M., Ettori S., Bartelmann M., Verdugo T., 2013, *Space Sci.Rev.*
- Mahdavi A., Hoekstra H., Babul A., Bildfell C., Jeltema T., Henry J. P., 2013, *ApJ*, 767, 116
- Meneghetti M., Bartelmann M., Dahle H., Limousin M., 2013, *Space Sci.Rev.*
- Meneghetti M., Fedeli C., Pace F., Gottlöber S., Yepes G., 2010a, *A&A*, 519, A90+
- Meneghetti M., Fedeli C., Zitrin A., Bartelmann M., Broadhurst T., Gottlöber S., Moscardini L., Yepes G., 2011, *A&A*, 530, A17+
- Meneghetti M., Rasia E., Merten J., Bellagamba F., Ettori S., Mazzotta P., Dolag K., Marri S., 2010b, *A&A*, 514, A93+
- Metcalf R. B., Madau P., 2001, *MNRAS*, 563, 9
- Morandi A., Pedersen K., Limousin M., 2010, *ApJ*, 713, 491
- Narayan R., Bartelmann M., 1996, ArXiv Astrophysics e-prints
- Navarro J. F., Frenk C. S., White S. D. M., 1996, *ApJ*, 462, 563
- Neto A. F., Gao L., Bett P., Cole S., Navarro J. F., Frenk C. S., White S. D. M., Springel V., Jenkins A., 2007, *MNRAS*, 381, 1450
- Newman A. B., Treu T., Ellis R. S., Sand D. J., 2011, *ApJ*, 728, L39+
- Newman A. B., Treu T., Ellis R. S., Sand D. J., Richard J., Marshall P. J., Capak P., Miyazaki S., 2009, *ApJ*, 706, 1078
- Oguri M., Bayliss M. B., Dahle H., Sharon K., Gladders M. D., Natarajan P., Hennawi J. F., Koester B. P., 2012, *MNRAS*, 420, 3213
- Oguri M., Takada M., 2011, *Phys.Rev.D*, 83, 023008
- Oguri M., Takada M., Okabe N., Smith G. P., 2010, *MNRAS*, 405, 2215
- Oguri M., Takada M., Umetsu K., Broadhurst T., 2005, *ApJ*, 632, 841
- Okabe N., Smith G. P., Umetsu K., Takada M., Futamase T., 2013, *ApJ*, 769, L35
- Okabe N., Takada M., Umetsu K., Futamase T., Smith G. P., 2010b, *PASJ*, 62, 811
- Planck Collaboration Ade P. A. R., Aghanim N., Armitage-Caplan C., Arnaud M., Ashdown M., Atrio-Barandela F., Aumont J., Baccigalupi C., Banday A. J., et al. 2013, ArXiv e-prints
- Postman M., Coe D., Benítez N., Bradley L., Broadhurst T., Donahue M., Ford H., Graur O., Graves G., Jouvel S., et al. 2012, *ApJS*, 199, 25
- Rasia E., Borgani S., Ettori S., Mazzotta P., Meneghetti M., 2013, *ApJ*, 776, 39
- Rasia E., Ettori S., Moscardini L., Mazzotta P., Borgani S., Dolag K., Tormen G., Cheng L. M., Diaferio A., 2006, *MNRAS*, 369, 2013
- Rasia E., Meneghetti M., Martino R., Borgani S., Bonafede A., Dolag K., Ettori S., Fabjan D., Giocoli C., Mazzotta P., Merten J., Radovich M., Tornatore L., 2012, *New Journal of Physics*, 14, 055018
- Redlich M., Bartelmann M., Waizmann J.-C., Fedeli C., 2012, *A&A*, 547, A66
- Rossi G., Sheth R. K., Tormen G., 2011, *MNRAS*, 416, 248
- Sereno M., Zitrin A., 2012, *MNRAS*, 419, 3280
- Shaw L. D., Weller J., Ostriker J. P., Bode P., 2006, *ApJ*, 646, 815
- Shaw L. D., Weller J., Ostriker J. P., Bode P., 2007, *ApJ*, 659, 1082
- Sheth R. K., Mo H. J., Tormen G., 2001, *MNRAS*, 323, 1
- Sheth R. K., Tormen G., 1999, *MNRAS*, 308, 119
- Umetsu K., Broadhurst T., Zitrin A., Medezinski E., Coe D., Postman M., 2011, ArXiv e-prints
- van den Bosch F. C., Tormen G., Giocoli C., 2005, *MNRAS*, 359, 1029
- Viola M., Melchior P., Bartelmann M., 2011, *MNRAS*, 410, 2156
- Zhao D. H., Jing Y. P., Mo H. J., Bnörner G., 2009, *ApJ*, 707, 354
- Zhao H., 1996, *MNRAS*, 278, 488
- Zieser B., Bartelmann M., 2012, ArXiv e-prints
- Zitrin A., Broadhurst T., Barkana R., Rephaeli Y., Benítez N., 2011, *MNRAS*, 410, 1939
- Zitrin A., Broadhurst T., Bartelmann M., Rephaeli Y., Oguri M., Benítez N., Hao J., Umetsu K., 2011c, ArXiv e-prints
- Zitrin A., Broadhurst T., Coe D., Umetsu K., Postman M., Benítez N., Meneghetti M., et al. M., 2011, *ApJ*, 742, 117
- Zitrin A., Menanteau F., Hughes J. P., Coe D., Barrientos L. F., Infante L., Mandelbaum R., 2013b, ArXiv e-prints
- Zitrin A., Meneghetti M., Umetsu K., Broadhurst T., Bartelmann M., Bouwens R., Bradley L., Carrasco M. e. a., 2013a, *ApJ*, 762, L30